Linear and nonlinear mechanisms within a forced plane wall jet

S. Bhatt and E. Gnanamanickam
Department of Aerospace Engineering, Embry-Riddle Aeronautical University, Daytona Beach, Florida 32114, USA

(Received 24 October 2019; accepted 21 May 2020; published 13 July 2020)

The plane wall jet (PWJ) was used as a model flow field to study the linear and nonlinear mechanisms within complex wall-bounded flows. Large-scale, large-amplitude forcing was used to introduce a "tracer" flow scale into the unforced base flow and the resulting embedded mechanisms were studied. The PWJ had a nominal Reynolds number $\mathrm{Re}_j = bV_j/\nu = 5965$ and was forced acoustically at a Strouhal number $\mathrm{St} = f_f b/V_j = 3.4\times10^{-3}$ and the resulting flow field was characterized at various downstream locations ($x/b \leqslant 162$) using hot-wire anemometry. Here, b is the PWJ exit slot width, V_j is the nominal PWJ exit centerline velocity, ν is the kinematic viscosity, and f_f is the forcing frequency. The forcing increased the outer length scale δ (increased spreading rate of the PWJ) along with a decrease in the outer velocity scale U_m and an increase in the local Reynolds number. The self-similarity of the mean streamwise velocity profile of the forced and unforced flow, respectively, was unaltered by the forcing, but the momentum in the wall region and the friction velocity were reduced along with a large increase in the streamwise turbulence in the wall region. The linear response of the PWJ to the forcing resulted in flow structures that have strong similarities to the naturally occurring structures of the unforced flow, both in the inner boundary layer and in the outer free-shear layer. A comparison of the energy spectra of the forced and unforced flow showed that the recipient scales, of the excess energy from forcing, were primarily the large scales in the wall region, with the specific scale of these recipient structures being that of the outer free-shear structures. At the upstream locations this energy transfer was primarily in the form of a forward cascade, while at downstream locations the transfer was in the manner of an inverse cascade. The nonlinear interaction between the large scales in the flow and finer scales was also found to be enhanced by the forcing. The spectra also suggested that the forcing isolated the energy transfer mechanism within the flow where the input energy was supplied at the forcing frequency. These observations led to the interpretation that the natural energy transfer mechanism within a PWJ is to transfer energy from the boundary layer coherent structures to the larger outer free-shear layer structures. The implications of these observations to modeling such complex wall-bounded flow fields, particularly considering the on-going work on the linear dynamics of the Navier-Stokes equation, were also discussed.

DOI: 10.1103/PhysRevFluids.5.074604

I. INTRODUCTION

A plane wall jet (PWJ) is formed when fluid from a two-dimensional nozzle exits into either quiescent fluid or an external costream, while the ensuing flow develops along a solid boundary or wall. The resulting shear flow thus has similarities to a free-shear layer in its outer extremities while the inner flow, constrained by the wall, has similarities to canonical boundary layers [1], namely, the zero-pressure gradient boundary layer and the fully developed channel flow. As an engineering flow field a PWJ is seen commonly in heating/cooling applications [2], for example, in the film cooling of turbine blades [3] and of internal electronics. It is encountered as well in the boundary

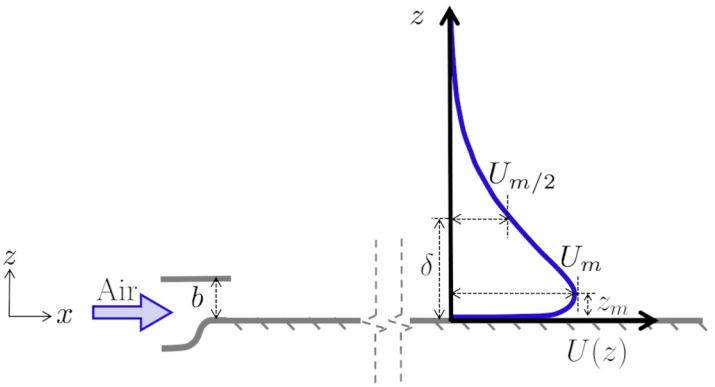

FIG. 1. A schematic highlighting the salient features of a PWJ velocity profile.

layer development of multielement airfoils [3,4]. The PWJ also has structural similarities to flows with a post-reattachment recovery region [5]. A number of past studies have focused on the mean turbulence statistics of the PWJ [3,4,6–10], while a few studies have emphasized the embedded structures [1,2,11–13].

Some characteristics of the PWJ are singular and motivate the present paper. The PWJ encapsulates boundary-layer-like flow structures as well as free-shear-like flow structures [1,11]. These structures are not restricted to their respective flow regions, but overlap with each other while also interacting with each other [1,2]. Further, within the PWJ the turbulence is produced at specific wall-normal regions, with turbulent transport playing a significant role in moving this turbulence to other flow regions where it is eventually dissipated [2,14]. Together, these characteristics result in a complex flow field which has proven challenging to model [15], due to the embedded dynamics, both linear as well as nonlinear. The present paper seeks to study these mechanisms, primarily from the view of scale energy transfer, with implications for modeling complex wall-bounded flows such as the PWJ. A brief background of these characteristics of the PWJ is now expanded upon along with an introduction to the present paper.

The PWJ has a streamwise mean velocity profile that reaches a maximum U_m at some distance z_m from the wall as shown in Fig. 1. The outer free-shear-like flow ($z > z_m$) and the inner boundary-layer-like flow ($z < z_m$) of the PWJ, as stated, are not merely superimposed on each other but the resulting flow encapsulates an overlap region with interactions between the two layers. This interaction is observed right from the onset of turbulence in the transitional region. Naqavi *et al.* [14] carried out a direct numerical simulation (DNS) of a PWJ up to a streamwise distance of $x/b = 43$. Here, x is streamwise ordinate while b is the PWJ exit slot height (see Fig. 1). They showed that the outer layer transitions via the inviscid Kelvin-Helmholtz (K-H) instability, where the characteristic spanwise K-H roller eddies eventually break down into smaller, complex structures. The inner wall layer transitions through a viscous process, under the influence of the outer layer, in a manner similar to bypass transition. This interaction between the outer free-shear layer structures and the near-wall turbulence is a structural feature of the PWJ which persists from the onset of turbulence into the fully turbulent region resulting in a single interacting flow field [1,2,13].

At further downstream distances, using a theory based on the asymptotic invariance principle George *et al.* [16] showed that at finite Reynolds number scaling solely based on viscous scales (ν/U_τ, U_τ) or outer scales (δ, U_m) cannot collapse the mean velocity or Reynolds stresses in the inner or outer region. Here, ν is the kinematic viscosity, $U_\tau = \sqrt{\tau_w/\rho}$ is the friction velocity, $\delta = z_{m/2}$ is the wall-normal location in the outer free-shear layer where the streamwise mean velocity is half the maximum velocity U_m (see Fig. 1), τ_w is the wall shear stress, and ρ is the fluid density. The implication to this scaling behavior then is that there exists an overlap region between the inner and outer region, for all finite Reynolds numbers, a zone in which mixed scaling is applicable. In

their large-eddy simulation (LES) study Dejoan and Leschziner [2] refer to this overlap region as the interaction region or zone. In this interaction region, where the outer structures overlap with the inner boundary layer, the turbulence kinetic-energy production is low. This region also lies between two peaks in the production, one in the inner wall layer and the other in the outer free-shear layer [2,12,14]. Naqavi *et al.* [14] showed that the inner wall layer budget of the turbulence kinetic energy and the Reynolds stresses, in both the spanwise and streamwise direction, were in general agreement with canonical boundary layers. However, there is an interaction between the inner and outer layers through triple velocity correlations. This interaction acts to transport turbulence energy from the outer layer to the inner one. The pressure-strain correlation then works to transfer this excess energy into the spanwise direction in the wall layer.

Two-point correlations reveal that the outer layer motions are large-scale, backward leaning structures [1,13]. Flow visualizations also reveal that these structures are associated with large-scale anticlockwise rotation [1]. On the other hand, the structures in the near-wall region are consistent with the forward leaning coherent motions seen in canonical boundary layers. The instantaneous snapshots from LES simulations also showed near-wall "streaky" structures consistent with structures associated with the near-wall cycle of canonical boundary layers [17]. Gnanamanickam *et al.* [1], using instantaneous particle image velocimetry fields and flow visualizations, showed that the near-wall region contains flow features that are consistent with packets of hairpin vortices similar to those seen in canonical wall boundary layers. The picture that then emerges is that the PWJ is an example of wall turbulence where, not surprisingly, the inner wall layer has structural features similar to canonical boundary layers. However, this inner wall layer is developing in the presence of energetic, large-scale, outer free-shear layer structures combined with an interaction between these two layers including embedded turbulent transport.

Motivated by these flow characteristics, the PWJ is used here as a model flow field to study the encapsulated mechanisms (both linear and nonlinear) within complex wall bounded flows, through the introduction of a specific "tracer" large scale. The approach followed is similar to that of McKeon and coworkers, who studied the nonlinear interactions within a zero-pressure gradient boundary layer through the introduction of synthetic, large-amplitude large scales [18–23]. Their synthetic scale was introduced via a dynamic surface roughness. The boundary layer responds to this forcing in a linear manner through streamwise modes at the forcing wavelength. Additionally, nonlinear interactions occur between triadically consistent wave numbers, as dictated by the nonlinear term in the Navier-Stokes equation, to distribute the excess energy from forcing.

As part of the present paper, the PWJ is altered through acoustic perturbations in the settling chamber of the incoming jet. This approach has been followed by Wygnanski and coworkers where studies of an acoustically perturbed PWJ were carried out [11,12]. Katz *et al.* [11] carried out a parametric study of a forced PWJ, without an external stream, over a range of Reynolds numbers ($\mathrm{Re}_j = bV_j/\nu = 3000$ to 30 000) and Strouhal numbers ($\mathrm{St} = f_f b/V_j = 3.4\times10^{-3}$ to 18.3×10^{-3}). Here, V_j is the PWJ exit centerline velocity and f_f the forcing frequency. They determined that the production in the near-wall region was reduced by the forcing with a concomitant reduction in wall shear stress exceeding 30%. In an associated study Zhou *et al.* [12] acoustically perturbed a PWJ in the presence of an external stream. The PWJ Reynolds number was $\mathrm{Re}_j = 6900$ while the forcing was at a single Strouhal number of $\mathrm{St} = 9.5\times10^{-3}$. The forcing frequency f_f was chosen to be the predominant frequency in the wall region of the unexcited PWJ at a downstream location of approximately $x/b = 100$. The forcing caused the turbulence intensity at the PWJ exit centerline to increase from 0.7 to 5%, indicative of large-amplitude perturbations. They determined that the wall shear stress was reduced by about 7% between streamwise distances $x/b = 100$ and 200. There was also a significant increase in the near-wall streamwise turbulence intensity near the surface when $x/b < 100$ which reduced at further downstream distances. At further downstream distances there was an increase in streamwise turbulence intensity away from the wall. They interpreted these two observations as a transfer of energy from the wall outwards. This contrasts with the recent DNS based observations where the natural mechanisms within a PWJ transferred outer large-scale energy to the near-wall region.

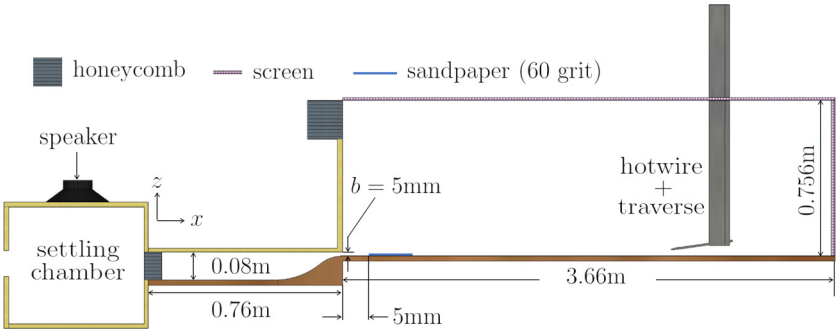

FIG. 2. A schematic highlighting the key features of the experimental facility and setup (not to scale).

Schober and Femholz [24] also studied a forced PWJ at a Reynolds number $\mathrm{Re}_j = 10\,000$. They used a still wire at the PWJ exit to break up the outer large scales which reduced the wall shear stress. They also used an oscillating wire (estimated Strouhal number $\mathrm{St} = 74.6\times10^{-3}$) which enhanced the outer layer structures with an associated reduction in wall shear stress. Together these studies all point to significant changes to the flow upon forcing, caused by changes in the internal mechanisms of the PWJ.

The present paper specifically considers large-scale ($\mathrm{St} = 3.4\times10^{-3}$), large-amplitude perturbations to the PWJ developing without an external stream at a nominal Reynolds number $\mathrm{Re}_j = 5965$. The present paper is not a parametric study but a detailed study focused on the response of the PWJ to a single forcing frequency f_f. Here, in contrast to the work of Zhou *et al.* [12], the forcing streamwise wavelength λ_x^f (based on Taylor's frozen hypothesis) was chosen to be large scale, in that for all streamwise distances considered $x/b \leqslant 162$, $\lambda_x^f > 2\delta$. It is sought to isolate (and track) the internal dynamics of the flow when an excess of energy is supplied at the forcing frequency. The context in which we present this paper is to understand the role of linear and nonlinear energy-transfer mechanisms within complex wall turbulence, with the long term goal being the ability to model and control these flow fields.

The paper is arranged as follows. First, the experimental approach is presented. A characterization of the forced flow is then presented, focusing on the changes to the mean turbulence statistics. The linear forcing response is then discussed, followed by changes to the energy spectra. Finally, the effect of forcing on the scale interactions within the flow is discussed, followed by a discussion on the implications of the present paper to current efforts at modeling wall turbulence. The paper is then concluded with a summary of key observations.

II. EXPERIMENTAL APPROACH

Measurements were conducted in a PWJ facility a schematic of which is shown in Fig. 2. Only a brief description of the facility is presented here and readers are referred to prior work [1] for a more detailed description. Air from a centrifugal blower passes through a series of filters and screens before entering a plenum settling chamber fitted with a speaker, to acoustically force the flow. From the plenum, air passes through a honeycomb section followed by a two-dimensional contraction channel of ratio 16:1 and exits through a rectangular nozzle. The nozzle height $b =$ 5 mm with an aspect ratio of 128. Past the jet exit, a 127-mm-long sandpaper strip (60 grit) is installed across the span of the facility which trips the flow. The trip was used to isolate the wall layer transition, as far as possible, from the outer layer structures and the imposed forcing. Past the exit the flow develops along a 3.66-m-long test section. The entrainment of the flow into the test section is conditioned using screens and honeycombs as shown in Fig. 2. The nominal jet exit Reynolds number $\mathrm{Re}_j = 5965$.

TABLE I. Experimental parameters of the HWA measurement campaign. Here the symbols used are as follows: x, streamwise location; b, PWJ exit height; $\mathrm{Re}_j = V_j b/\nu$, PWJ exit Reynolds number; V_j, PWJ exit velocity; ν, kinematic viscosity; U_m, maximum mean velocity; U_τ, friction velocity; z_0, point nearest to the wall used to calculate the friction velocity; $\mathrm{Re}_\tau = U_\tau \delta/\nu$, friction Reynolds number; δ, outer length scale; ν/u_τ, viscous length scale; C_{f_j}, friction coefficient based on the PWJ exit velocity; l, length of the hot-wire sensing element; T, the sampling time; d, hot-wire sensor diameter; $\Delta T = 1/f_s$, sampling period; $f_s = 20$ kHz, sampling frequency; and $f_c = U_\tau^2/3\nu$, maximum flow frequency [25]. The superscript $+$ is used to denote nondimensionalization using inner scales. The superscript $*$ indicates the forced cases.

x/b	Re_j	V_j (ms^{-1})	U_m (ms^{-1})	δ (cm)	U_τ (ms^{-1})	z_0^+	U_τ/ν (μm)	Re_τ	C_{f_j}	l^+	l/d	TU_m/δ	ΔT^+	f_c (kHz)
50	5902	17.83	5.90	3.47	0.3833	4.20	40	868	9.24×10^{-4}	25	200	40755	0.4801	3.2
50*	5896	17.81	5.36	4.28	0.3580		43	999	8.08×10^{-4}	23	200	30040	0.4184	2.8
75	5933	17.85	4.81	4.77	0.3325	4.26	46	1038	6.94×10^{-4}	22	200	33290	0.3607	2.4
75*	5929	17.84	4.50	5.88	0.3132		49	1204	6.17×10^{-4}	20	200	25244	0.3201	2.1
110	5994	17.98	4.18	6.77	0.2700	4.02	56	1199	4.46×10^{-4}	9.8	216	25967	0.2425	1.6
110*	5994	17.98	3.85	8.17	0.2495		61	1332	3.85×10^{-4}	9	216	19787	0.2045	1.4
137	6020	18.06	3.73	8.11	0.2471	4.20	62	1315	3.73×10^{-4}	9	216	22068	0.2002	1.3
137*	6020	18.06	3.43	9.93	0.2293		67	1489	3.23×10^{-4}	8.9	216	16568	0.1728	1.2
162	5972	18.00	3.62	9.46	0.2261	4.10	68	1396	3.08×10^{-4}	8	216	18354	0.1669	1.1
162*	5992	18.00	3.31	11.08	0.2038		75	1481	2.57×10^{-4}	8.1	216	14314	0.1355	0.9

Measurements were conducted using single hot-wire anemometry (HWA). The hot-wire sensors had a nominal diameter $d \approx 2.5$ μm and the aspect ratios of the sensors for all measurements were ensured to be $l/d \approx 200$ to minimize attenuation [25]. The overheat ratio of the HWA sensor was 1.8. Wall-normal measurements were carried out at streamwise distances $x/b = 1$ to 162. A linear magnetic encoder was used to track the motion of the hot-wire sensor at a resolution of $\approx$1 μm. At each streamwise location measurements were carried out at 75 wall-normal positions. The first 15 points were equidistant from each other ($\approx$13 μm) and are nominally in the very-near-wall region ($z^+ < 15$). These points are used to calculate the wall shear stress or friction velocity. A more detailed description of the wall shear stress measurement technique, which is based on a near-wall curve fit, is given in Gnanamanickam *et al.* [1]. Past these equidistant locations, measurements were carried out at 60 logarithmically spaced wall-normal positions. Table I summarizes the measurement parameters for all measurements presented. The wall shear stress and subsequently the friction velocity U_τ were measured by curve fitting the near-wall mean streamwise velocity $\overline{U}$, between wall-normal locations $z^+ \approx 4$ and 10, as described in Gnanamanickam *et al.* [1]. The measurement location closest to the wall for each data set is also shown in Table I.

At each wall-normal measurement station, measurements were first carried out on the unforced PWJ. Following this, a pulse wave with a width of 1 ms at the forcing frequency (f_f =12 Hz, $\mathrm{St} = 3.4\times10^{-3}$) was fed to the speaker, through an amplifier, to generate the forcing input. This pulse wave was also used as the reference signal while calculating the phase-locked velocity fields presented in a subsequent section. Measurements were then carried out at this wall-normal location for the case of the forced flow. Following this the speaker was turned off and the hot-wire sensor was traversed to the next wall-normal location and the process was repeated at subsequent wall-normal locations. The entire process including the data acquisition was automated.

III. RESULTS

The following conventions are followed while comparing the forced and the unforced flows. Red lines and symbols are used to depict forced quantities while black lines and symbols are used to represent unforced quantities. To carry out comparisons between various streamwise locations most

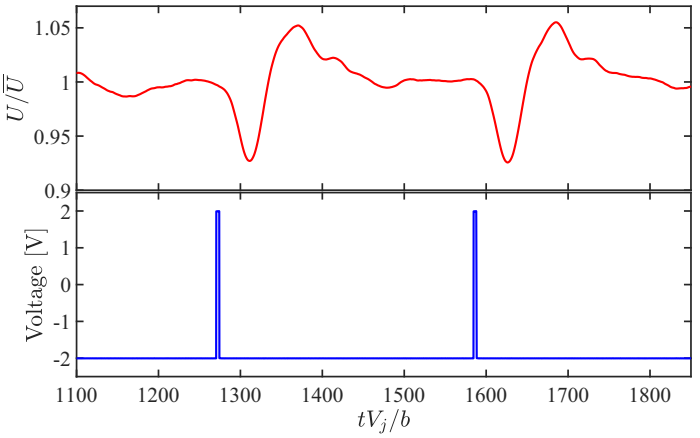

FIG. 3. Instantaneous velocity of the forced flow at the PWJ exit ($x/b = 1$) centerline (top). The corresponding input signal to drive the speaker, in the settling chamber, is also shown (bottom).

quantities are nondimensionalized using jet exit conditions; i.e., the length scale is the PWJ jet exit width b and the velocity scale is the nominal PWJ exit centerline velocity V_j. Normalizations based on inner and outer scaling are also used where appropriate. The superscript zero is used to indicate unforced quantities while the asterisk superscript is used to indicate forced quantities.

Through the course of the following discussion three wall-normal locations, at each streamwise station, are used to highlight keys changes to the flow field. These wall-normal locations are (i) $z^+ \approx 15$, (ii) $z^+ \approx 60$, and (iii) $z \approx 0.6\delta^0$. In figures, these locations are highlighted using line styles as described in the caption of Fig. 8(a). The region around the nominal wall-normal location $z^+ \approx 15$ is referred to as the near-wall region. The wall-normal locations $z^+ \approx 15$ and 60 are less than z_m, the location of the maximum mean velocity U_m. The wall-normal region that contains both these wall-normal locations, i.e., $z < z_m$, is broadly referred to as the wall region. The wall-normal region around $z \approx 0.6\delta^0$ is then broadly referred to as the outer region (for the outer free-shear region). To convert Fourier components f of the velocity field into a streamwise wavelength λ_x the outer velocity scale of the unforced PWJ is used, i.e., $\lambda_x = U_m/f$.

A. Forcing response at the PWJ exit

An acoustic excitation was used to introduce a large-scale, large-perturbation forcing into the flow field. A portion of the forced velocity signal at the PWJ exit ($x/b = 1$) centerline is shown in Fig. 3 (top). The speaker was located in the settling chamber (see schematic of Fig. 2). Hence, the flow passes through a honeycomb section and the contraction past the location of actuation. Thus, the instantaneous velocity shown in Fig. 3 is the result of the forcing, combining the effects of the actuation passing through the honeycomb and contraction. For the purpose of this paper the goal was in generating a flow field with energetic large scales at the forcing frequency, which the spectra, presented in subsequent sections, show has been achieved. The driving input signal to the speaker is also shown in Fig. 3 (bottom) for reference. At the PWJ exit centerline, the forcing increased the turbulence intensity from 0.7 to 1.8%, while in the outer shear layer it increased from 11.1 to 18.2%. At the wall-normal location closest to the wall ($z \approx 100$ μm) the forcing increased the turbulence intensity from 4.3 to 9.8%. Figure 3 shows that the introduced forcing has a distinct large-scale component while the changes in turbulence intensity establish that the forcing is a large perturbation to the base flow.

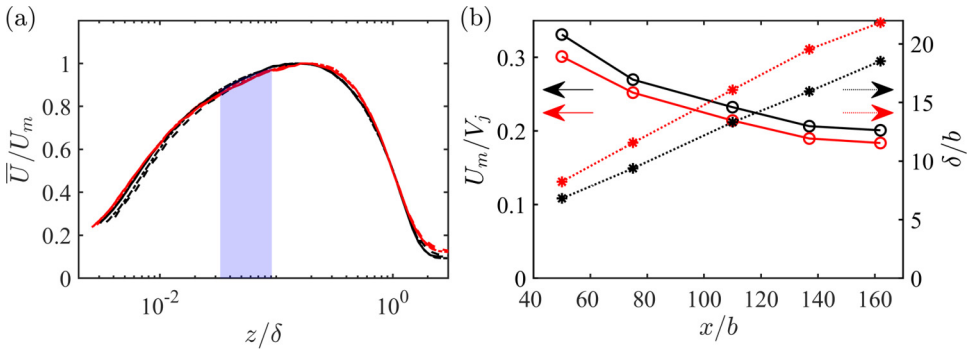

FIG. 4. (a) Comparison of the streamwise mean velocity profiles nondimensionalized using outer scales at $x/b = 75$ (- - - - -), 110 (·····), and 162 (———) respectively. The shaded region highlights the nominal logarithmic region of the unforced flow at $x/b = 110$. (b) Outer length scale δ (·····) with values represented on the right y axis and velocity scale U_m (———) with values represented on the left y axis, as a function of streamwise distance. Black lines and symbols are used to represent unforced quantities whereas red lines and symbols are used to show forced quantities.

B. Turbulence statistics

The PWJ has been shown to have a self-similar streamwise mean velocity profile past the initial transitional stage downstream of the exit [6]. Typical self-similar velocity profiles of the unforced flow at various downstream locations are shown in Fig. 4(a). Figure 4(a) also compares the velocity profile of the unforced PWJ with that of the forced one, in outer scaling. The forcing results in a velocity profile that is still self-similar while considering the forced and unforced flow individually. The forced flow also shows similar outer scaling behavior as the unforced PWJ. Also seen is a limited logarithmic region (shaded region) for both the forced and unforced flow in the wall region, below the location of the maximum velocity U_m. This logarithmic region was observed to increase in extent with increasing downstream distance (not shown here for brevity). Figure 5 shows the streamwise development of the mean velocity profiles of both the forced and the unforced flows. A closer view of the streamwise velocity and the turbulence intensities, showing the region around

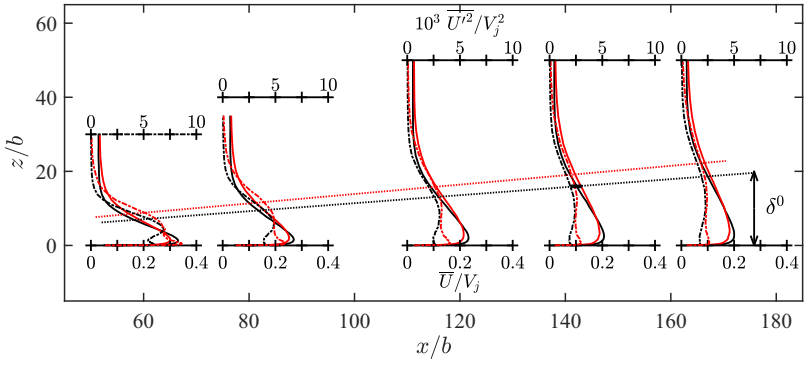

FIG. 5. Development of the streamwise mean velocity (———) and turbulence intensity (–·–·–·–) profiles of unforced and forced flow. Also shown are the respective developments of the shear-layer thickness δ (·····). Black lines are used to represent unforced quantities whereas red lines are used to show forced quantities. Figures 20 and 21 in Appendix A show zoomed-in profiles of the mean streamwise velocity and turbulence intensity, respectively.

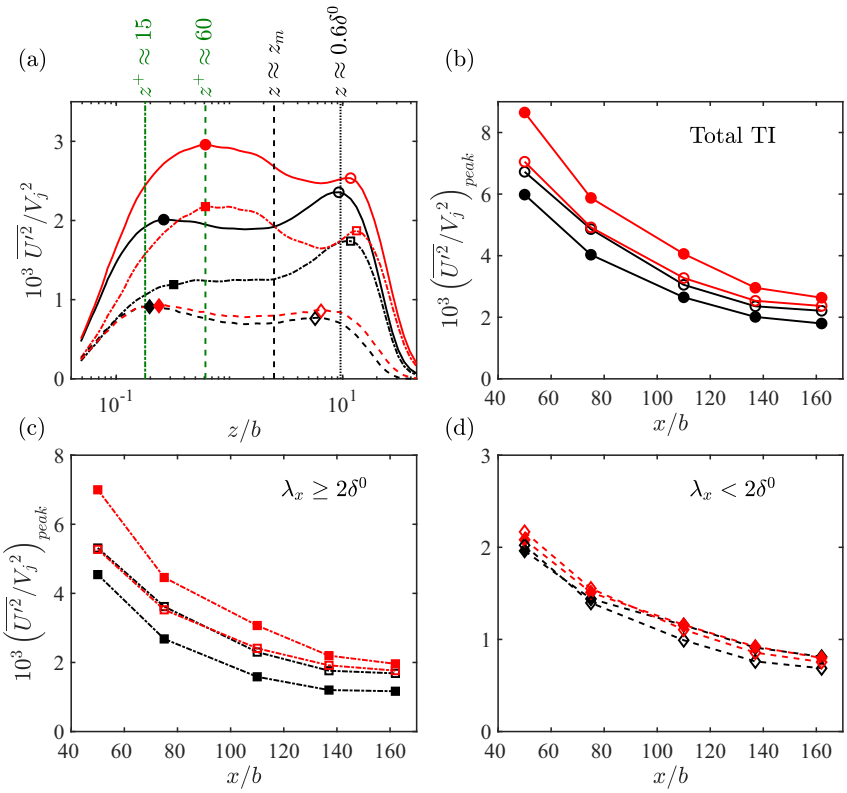

FIG. 6. (a) Streamwise turbulence intensity (TI) profile at $x/b = 137$. The vertical lines indicate wall-normal locations $z^+ \approx 15$ (-·-·-·-), $z^+ \approx 60$ (- - - - -), $z \approx z_m$ (- - - - -), and $z \approx 0.6\delta^0$ (·····), respectively. The total TI (——) along with its large-scale component (-·-·-·-) and small-scale component (- - - - -) are shown. The filled symbols mark the inner peaks of the total TI (●), large-scale TI (■), the small-scale TI (◆), respectively. The unfilled symbols mark the outer peaks of the total TI (○), large-scale TI (□), and small-scale TI (◇), respectively. (b)–(d) The variation of the inner and outer peaks as a function of streamwise distance corresponding to (b) the total TI, (c) the large-scale TI, and (d) the small-scale TI peaks, respectively. While comparing forced and unforced quantities black lines and symbols are used to represent the unforced quantities whereas red lines and symbols are used to show forced quantities.

U_m, is reproduced in the Appendix A for clarity. In both cases, as the PWJ develops downstream the maximum mean velocity U_m decreases and the outer length scale δ increases. At a fixed streamwise location, the effect of forcing is to reduce the outer velocity scale which is the maximum mean velocity U_m, while increasing the outer length scale δ. This trend is observed at all streamwise locations considered. This variations of U_m and δ as a function of streamwise distance, for both the forced and the unforced cases, are shown in Fig. 4(b). The spreading rate of the PWJ when forced increased from $d\delta^0/dx \approx 0.105$ to $d\delta^*/dx \approx 0.123$ indicating a 17% increase, as evident from the diverging lines of constant δ in Fig. 5. It is noted that one standard deviation in determining δ was estimated to be ± 0.61 mm. Together the increase in δ and the reduction in U_m resulted in an increase in the local Reynolds number $\mathrm{Re}_m = U_m\delta/\nu$, upon forcing.

The typical streamwise turbulence intensity profile in the fully developed region (at $x/b = 137$) is shown in Fig. 6(a). The streamwise turbulence intensity profile of the PWJ has two peaks. The inner peak in the near-wall region is associated with near-wall structures whereas the outer peak is associated with the outer free-shear layer structures with some overlap of scales. The streamwise development of the streamwise turbulence intensity profiles is also shown in Fig. 5. The variations

in magnitudes of the inner and outer peaks are shown in Fig. 6(b). As expected, both the peaks gradually reduce in the magnitude as the PWJ develops downstream in the case of the forced and unforced PWJ. In the case of the unforced PWJ the inner peak is always smaller in magnitude than the outer peak for all streamwise locations considered. On average, the outer peak in the unforced PWJ is approximately 16.6% larger than the inner peak. However, in the case of the forced PWJ, the inner peak is higher in magnitude than the outer peak; i.e., the forcing increases the inner peak by ≈52.8% across all streamwise locations considered. There is also a slight but not as substantial increase in the magnitude of the outer peak in the case of the forced PWJ (≈4.6% on average across all streamwise locations). This indicates that the forcing response of the PWJ appears to primarily affect the inner wall layer, increasing the streamwise turbulence intensity substantially.

The total turbulence intensity profile indicates the turbulence activity integrated across all wavelength components. To get a clearer view of the forcing response, Fig. 6 also shows the turbulence intensity profiles at $x/b = 137$ decomposed into its large-scale and small-scale components. Here, large scales are defined as scales with streamwise wavelength $\lambda_x > 2\delta^0$. The choice of $\lambda_x = 2\delta^0$ as the cutoff wavelength was made to be consistent with past work, where the implications of this choice are discussed [1]. This cutoff wavelength is chosen with the understanding that some leakage between scales is inevitable due to the extremely energetic outer large scales in the flow, their intrusion into the wall region, and the modest friction Reynolds numbers under consideration. It is noted that the precise choice of the cutoff wavelength does not affect the qualitative conclusions that follow from separating flow scales into large scales and small scales. In all subsequent discussions, where the flow is separated into large scales and small scales, a spectral cutoff filter was used to separate the large scales from the small scales. The large scales are seen to be primarily responsible for the larger outer peak in the unforced PWJ. A peak in the small-scale intensity is also seen in the outer free-shear layer. On the other hand, in the inner wall layer, a peak in both the large-scale and small-scale turbulence intensity is observed. In the case of the unforced PWJ, these two peaks contribute almost equally to the turbulence intensity. In the case of the forced PWJ there is virtually no change in the small-scale turbulence intensity due to forcing. However, there is an increase in the large-scale intensity across the entire flow layer. This increase is maximum around the wall-normal location $z^+ \approx 60$. This location lies within the logarithmic region of the mean velocity profile [see Fig. 4(b)].

The differences between the forced and the unforced PWJ at other streamwise locations are well represented by the described behavior at $x/b = 137$. This is also highlighted in Fig. 6, where the streamwise variations of the inner and outer peaks separated into a small-scale peak and a large-scale peak are shown. Across all streamwise locations considered the large scales contribute ≈75.9% to the outer turbulence intensity peak and ≈65.4% to the inner peak in the case of the unforced PWJ; i.e., the large scales make a larger contribution towards the outer peak. However, upon forcing, the large-scale contribution to the outer peak is ≈74% and it is ≈76.2% towards the inner peak. This highlights that the imposed perturbation is a large-scale forcing with the wall region being the primary target region.

C. Skin friction coefficient and PWJ momentum

The streamwise variations of the skin friction coefficient $C_{f_j} = 2U_\tau^2/V_j^2$ for the unforced and the forced flows are shown in Fig. 7(a). The forcing reduces the friction coefficient at all streamwise locations considered. On average the reduction in C_{f_j} is observed to be ≈13.5%. It is noted here that the reduction in U_τ is combined with an increase in δ. Together these changes to the flow increase the local friction Reynolds number $\mathrm{Re}_\tau = \delta U_\tau/\nu$ upon forcing. Numerical values of Re_τ are tabulated in Table I.

At a given streamwise location the PWJ mean momentum M_j is split into its contributions from the wall region and the outer region as

$$M_j = \int_0^{z_m} \overline{U}^2 dz + \int_{z_m}^{2.5\delta} \overline{U}^2 dz. \tag{1}$$

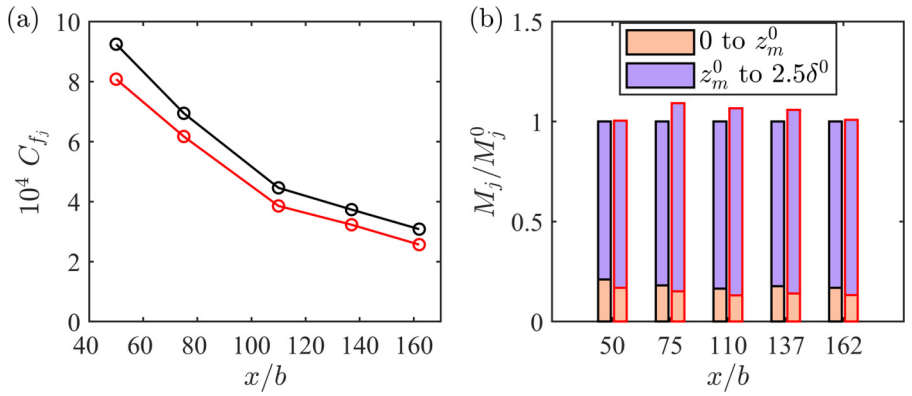

FIG. 7. (a) Variation of the skin friction coefficient $C_{f_j} = 2U_\tau^2/V_j^2$ (—o—) as a function of streamwise distance. While comparing forced and unforced flows black lines and symbols are used to represent the unforced quantities whereas red lines and symbols are used to show forced quantities. (b) Variation of the PWJ momentum as a function of streamwise distance decomposed into its contributions from the wall ($z < z_m$) and the outer ($z \geqslant z_m$) regions. These are nondimensionalized with respect to the total unforced momentum M_j^0 as per Eq. (1). The outline around the bars is used to differentiate between the unforced (black) and the forced (red) flows.

Here, z_m is the wall-normal location of the outer velocity scale U_m and is used to distinguish the inner wall layer and the outer free-shear layer. Figure 7(b) shows the PWJ mean momentum as a function of streamwise location split into its contributions from the inner wall layer ($z < z_m$) and the outer free-shear layer ($z \geqslant z_m$). The forcing increases the total PWJ momentum substantially when $x/b = 75$–137. The increased momentum is maximum at $x/b = 75$ and gradually decreases as the flow develops further downstream. However, this increase in momentum occurs in the outer free-shear layer region ($z > z_m$). In contrast the forcing reduces the momentum in the wall region ($z < z_m$) coincident with the decrease in U_m. It is noted here that z_m also increases upon forcing similar to the outer length scale δ. One explanation for the decrease in the wall region momentum is that the forcing causes the turbulent transport of higher momentum fluid away from the wall region into the outer free-shear layer. This decrease in the near-wall momentum will also occur when there is an increase in the entrainment of the external still (low momentum) fluid into the free-shear layer which is then subsequently transported to the near-wall region. As subsequent sections reveal, large-scale structures in the flow are energized by the forcing, leading to large-scale mixing in the flow. Hence, in the presence of large-scale mixing, it is likely that both these processes (transport of higher momentum fluid away from the wall and external lower momentum fluid towards the wall) occur simultaneously, leading to a reduction in the mean momentum in the wall region and subsequently a reduction in the skin friction.

D. Forcing response at $x/b = 50$

A sandpaper strip was used to trip the inner wall layer in the case of both the forced and the unforced flow as described in the section focusing on the experimental setup. The streamwise location $x/b = 50$, which is $24b$ downstream of the sandpaper strip, is past the initial PWJ development region where the unforced flow becomes two dimensional. As the streamwise location $x/b = 50$ is the most upstream location, past the initial development phase, we consider this location as the "initial" forcing location with respect to further downstream locations $x/b > 50$. The spectrograms of the unforced and forced flow at $x/b = 50$ are shown in Figs. 8(a) and 8(b) respectively. Here, spectrogram refers to the contours of the premultiplied, one-dimensional, streamwise energy spectra

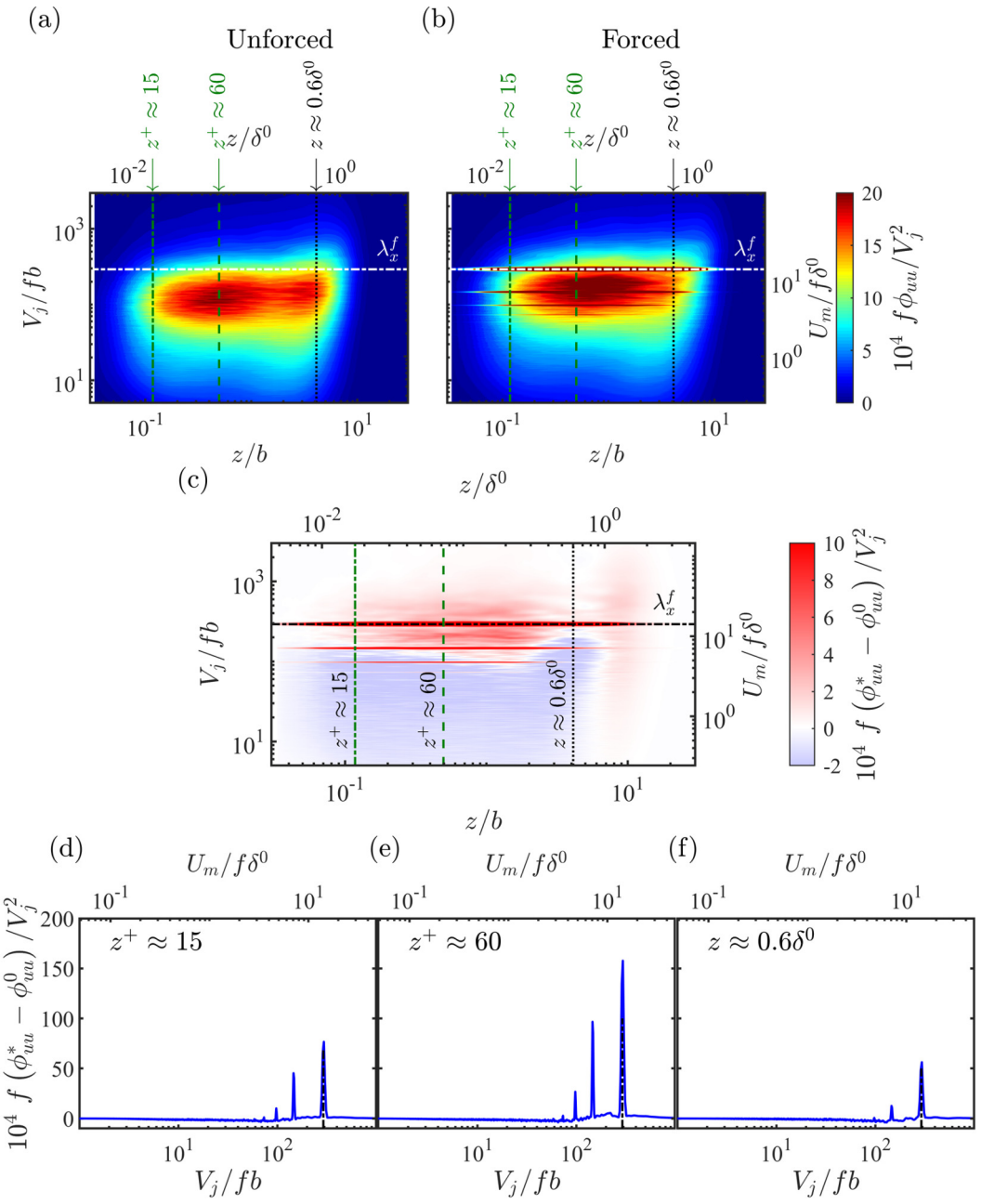

FIG. 8. Spectrogram at $x/b = 50$ for the (a) unforced and (b) forced flows as well as the (c) difference between the two spectra. The vertical lines show the wall-normal locations $z^+ \approx 15$ (–·–·–·–) and 60 (– – – – –) and $z = 0.6\delta^0$ (·····). (d)–(f) Profiles of the difference in energy spectra at the three highlighted wall-normal locations. Shown also for reference is the forcing wavelength $V_j/f_f b \approx 295$ (–·–·–·–).

$f\phi_{uu}$ as a function of wall-normal distance z/b and streamwise wavelength V_j/f, where f are the Fourier frequency components of the streamwise velocity fluctuations U'.

The differences between the two spectrograms are highlighted in the difference plot of Fig. 8(c) while the differences at the three highlighted wall-normal locations are presented in Figs. 8(d)–8(f).

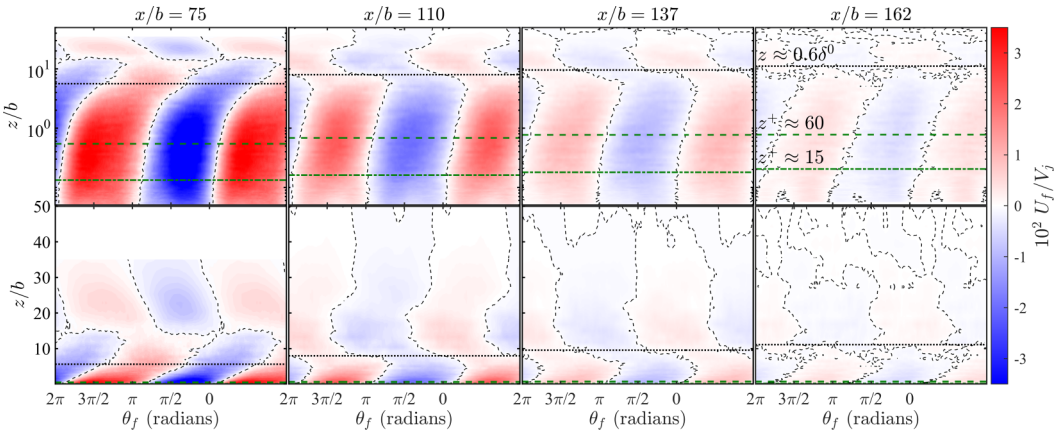

FIG. 9. Variation of the phase-locked velocity U_f [see Eq. (2)] over two forcing cycles shown in logarithmic (top) and linear (bottom) wall-normal coordinates. The streamwise distance increases going from left to right. The color contours are the magnitude of U_f as indicated by the color bar. The contour level corresponding to $U_f = 0$ is also shown. The horizontal lines show wall-normal locations $z^+ \approx 15$ (-·-·-·-) and 60 (- - - - -) and $z = 0.6\delta^0$ (·····), respectively.

A peak in $f\phi_{uu}$ at the fundamental forcing frequency f_f as well as several higher harmonics are seen. In the wall region ($z^+ \approx 15$ and $\approx$60) four higher harmonics are seen. On the other hand in the outer region ($z \approx 0.6\delta^0$) only two higher harmonics are seen. Apart from the forcing frequency and its harmonics, Fig. 8(c) shows that the forcing increases the energy of all flow scales in the outer extremities of the PWJ ($z \gtrapprox 0.6\delta^0$). In the wall region, the increase in energy is limited to scales larger than $V_j/fb > 10^2$ (or $\lambda_x = U_m/f > 6\delta^0$) while for smaller scales the forcing decreases the energy. These changes point to large-scale transport within the forced PWJ upon forcing. The spectral development of the forced and unforced PWJ is now compared at further downstream locations $x/b = 75$–162.

E. Forcing harmonic response

As the imposed forcing was a periodic function, following past studies [21–23,26], the velocity field was triple decomposed into a mean velocity component $\overline{U}$, a periodic phase-locked component U_f that was phase locked with the imposed forcing, and an unsteady fluctuating component U_f':

$$U(z,t) = \overline{U(z)} + U_f(z,t) + U_f'(z,t). \tag{2}$$

For the rest of this paper, the term phase-locked velocity is used to refer to U_f. The input signal to the speaker, as part of the forcing (see Fig. 3), was used as the reference signal while carrying out the phase-locking procedure. Using this reference, an ensemble average in phase θ_f of the mean subtracted velocity field was carried out at each wall-normal location z and a two-dimensional map of U_f was subsequently calculated. The unsteady component U_f' then represents the background turbulent fluctuations about this periodic phase-locked component and the mean velocity field $\overline{U}$. The phase-locked velocity U_f calculated in this manner captured the linear response of the flow, to the forcing, as well as the higher harmonics.

Figure 9 shows contours of U_f (over two forcing cycles) as a function of downstream distance. As discussed, Fig. 9 captures the flow response at the fundamental forcing frequency f_f, which is the linear response of the PWJ to the forcing [23]. It also captures some of the nonlinearities of the response in the form of higher harmonics. A filtered version of Fig. 9 is shown in Appendix B (Fig. 22) where only the linear response portion of U_f was isolated. Here, prior to

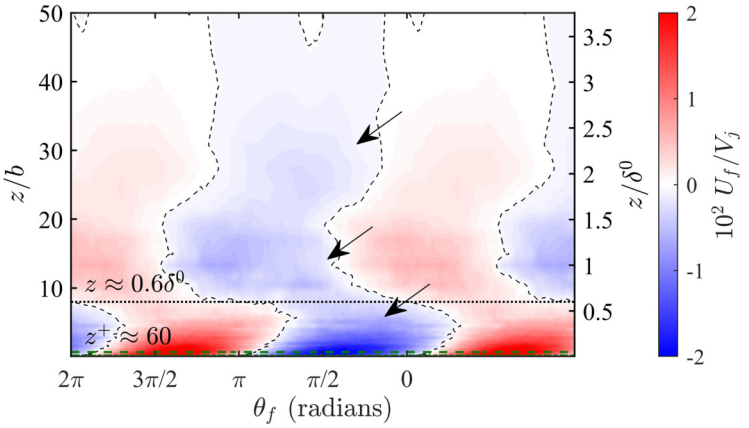

FIG. 10. Variation of the phase-locked velocity U_f [see Eq. (2)] over two forcing cycles in linear wall-normal coordinates at $x/b = 110$. The color levels represent the magnitude of U_f as indicated by the color bar. The contour level corresponding to $U_f = 0$ (- - - - -) is also shown. The horizontal lines show the wall-normal locations $z^+ \approx 60$ (- - - - -) and $z = 0.6\delta^0$ (·····), respectively. The arrows highlight the three distinct flow features discussed in the text.

the phase-locking procedure the mean subtracted velocity field was bandpass filtered about the fundamental ($f_f \pm 0.01$Hz) to isolate the linear response. Comparing both figures, it is seen that the large-scale flow features of Fig. 9 are those of the linear response. Higher harmonics are seen primarily in the wall region particularly at the upstream locations ($x/b < 110$). These harmonics are also highlighted in the discussion of the spectra in a subsequent section.

The linear response at $x/b = 110$ is shown in Fig. 10 to highlight key elements. At this streamwise location the periodic response has three distinct features that span the wall-normal region (highlighted by the three arrows). In the region closest to the wall ($z \lessapprox 0.6\delta^0$) the response is a forward leaning (positive inclination angle) flow feature. This response flow feature is "attached" to the wall, in that its footprint extends down to the wall. This inner response also extends well past z_m, the location of the maximum local mean velocity U_m. In the outer extremities of the flow ($z \gtrapprox 0.6\delta^0$), two other features are seen. The central flow feature extends to about $z \approx 1.5\delta^0$ while the other feature extends past $z \approx 1.5\delta^0$. The response flow feature spanning the wall-normal region $0.6\delta^0 \lessapprox z \lessapprox 1.5\delta^0$ shows a negative inclination angle (backward leaning). At this streamwise location the outermost feature has an inclination angle nearly aligned with the vertical.

Considering the downstream development of the phase-locked velocity U_f, it is evident that the magnitudes of these response flow features seen in the contours of U_f reduce with increasing downstream distance. In other words, the energy at the forcing frequency is being depleted as the flow develops downstream. The three flow features of the linear response, highlighted in Fig. 10, are observed at all downstream ($x/b > 75$) locations considered. However, the relative phase between them changes with downstream distance. Here, relative phase indicates the phase between any two of the three flow features highlighted in Fig. 10. For example, the relative phase between the innermost wall response feature and the central one is highlighted as ψ in Fig. 22 of Appendix B. This change in relative phase indicates that these distinct response features, as highlighted in Fig. 10, are convecting at different velocities as the flow develops downstream. For example, the relative phase between the innermost response feature and the central one ψ has increased as the flow develops downstream (see Fig. 22 of Appendix B). The innermost flow feature has a constant forward inclination angle. The middle flow feature shows a negative inclination angle at all streamwise locations. However, the outermost flow feature exhibits a small negative inclination angle at $x/b = 75$ and 110 and transitions into a flow feature with a small positive inclination angle

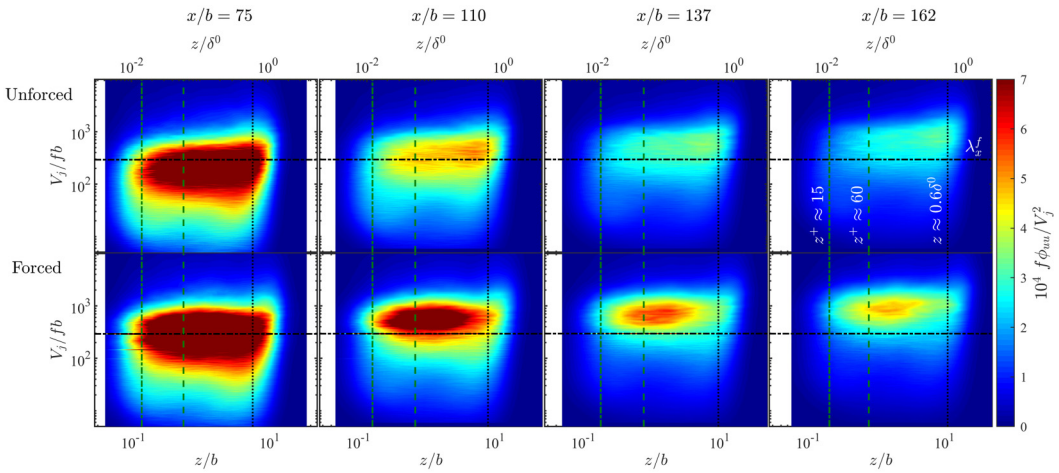

FIG. 11. Spectrograms of the unforced (top) and the forced (bottom) flows. The streamwise development is shown from left to right. The vertical lines show the wall-normal locations $z^+ \approx 15$ (-·-·-·-) and 60 (- - - - -) and $z \approx 0.6\delta^0$ (·····), respectively. The horizontal line shows the forcing wavelength $V_j/f_f b$ (-·-·-·-).

at $x/b = 162$. At the most upstream streamwise location ($x/b = 75$), the two inner flow features also appear to be merged into a single flow feature.

It is also highlighted that the strength or magnitude of the innermost response feature, i.e., the forward leaning attached one, is consistently higher than the outer ones. This is true at all streamwise locations as indicated by the color contours in Fig. 9. Several recent studies have focused on the linear response of the Navier-Stokes equation [18,27,28]. In this context, the current paper presents the linear response of a flow to forcing with an added degree of complexity than canonical wall turbulence. The linear response in the wall region that is forward leaning and the free-shear layer response which is backward leaning bear strong resemblance to the structures captured by the two-point correlations of Gnanamanickam *et al.* [1] in the respective flow regions of the unforced flow. In other words, the linear response of the forced PWJ results in flow features that mimic the naturally occurring structures in the PWJ at the forcing wavelength. The greater strength of the wall layer linear response when compared with that in the free-shear layer may suggest that the linear gain of the near-wall structures, at the particular forcing frequency, is higher in the initial flow development stage close to the PWJ exit ($x/b < 50$). However, it is cautiously noted that the strength of these response features, as visualized using a phase averaging process, will be affected by any phase jitter.

F. Energy spectra

The streamwise spectral evolution of the forced and unforced flow is shown in Fig. 11 in the form of spectrograms. For reference, the spectra corresponding to Fig. 11 using Taylor's hypothesis and the local mean velocity as the convection velocity are shown in Appendix C (Fig. 23). Line plots of the one-dimensional, premultiplied, streamwise energy spectra at the aforementioned three wall-normal locations $z^+ \approx 15$ and 60 and $z \approx 0.6\delta^0$ are shown in Fig. 12 to also aid in the discussion of the spectra.

The spectrograms of the unforced PWJ are first considered. To highlight key features, the unforced spectrogram at $x/b = 137$ is shown in Fig. 13. It is noted that the features of the unforced PWJ discussed at $x/b = 137$ are exemplary of all other streamwise locations considered [see also the spectrogram of Fig. 8(a) at $x/b = 50$]. At all streamwise locations, the PWJ encapsulates highly energetic large-scale structures ($\lambda_x > 2\delta^0$) which span the entire wall-normal extent of the PWJ.

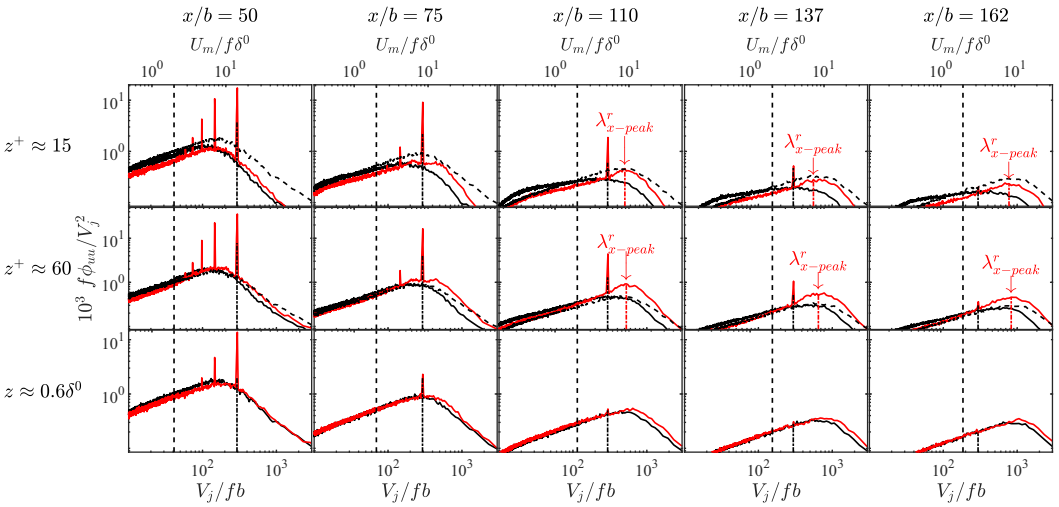

FIG. 12. Comparison of the streamwise, one-dimensional, premultiplied energy spectra $f\phi_{uu}/V_j^2$ (———) at a near-wall location $z^+ = 15$ (top), a logarithmic location $z^+ = 60$ (middle), and an outer location $z = 0.6\delta$ (bottom) (corresponds to the locations highlighted in Fig. 11). At the wall layer locations $z^+ \approx 15$ and 60, the outer unforced spectrum from $z \approx 0.6\delta^0$ (- - - - -) is also plotted for a comparison. The black color represents unforced quantities while the red color represents forced quantities. The vertical lines show the cutoff wavelength $\lambda_x = 2\delta^0$ (- - - - -) and the forcing wavelength $V_j/f_f b$ (-·-·-·-), respectively. Also shown are the peaks of the recipient scales $\lambda^r_{x-\mathrm{peak}}$ (-·-·-·-) in the wall layer when $x/b \geqslant 110$.

Note, in Figs. 11 and 12 a line is used to highlight the spatial differentiator wavelength $\lambda_x = 2\delta^0$ at each streamwise location. Though this large-scale energy resides at all wall-normal locations it is particularly energetic at two wall-normal regions. At the streamwise location $x/b = 137$ these two regions are highlighted as the shaded regions in Fig. 13. The first of these regions lies between $z \approx 0.01\delta^0$ and $0.12\delta^0$. These are the wall-normal locations nominally spanning the logarithmic region of the inner wall layer [see Fig. 4(a)]. This region lies below z_m, the wall-normal location of the maximum mean velocity U_m. For the rest of this paper the large-scale wavelengths that reside in this first region are referred to as λ^n_{xi}, i.e., λ^n_{xi} represents the naturally occurring large scales that are observed in the PWJ between the wall-normal locations $0.01\delta^0 \lessapprox z \lessapprox 0.12\delta^0$ or the inner wall region.

The second region where large-scale energy is concentrated is around the wall-normal location $z \approx 0.6\delta$. This wall-normal location lies in the outer free-shear portion of the PWJ and for the rest of this paper these outer large-scale wavelengths are referred to as λ^n_{xo}. It is emphasized that λ^n_{xo} and λ^n_{xi} are not single wavelengths but a range of energetic large-scale wavelengths, each with a peak that varies with wall-normal distance (see Figs. 13 and 12). In the case of the unforced PWJ the concentration of energy is greater in this second outer region when compared with the inner region for all streamwise locations considered. Further, the wavelength corresponding to the peak in energy of all wavelengths comprising λ^n_{xo} is greater than the peak wavelength of λ^n_{xi}, i.e., $\lambda^n_{xo-\mathrm{peak}} > \lambda^n_{xi-\mathrm{peak}}$. Here, $\lambda^n_{xo-\mathrm{peak}}$ is the wavelength in the outer region where the large-scale energy is a maximum and likewise $\lambda^n_{xi-\mathrm{peak}}$ is that in the inner region [see Fig. 13(c)].

The forced PWJ is now considered. Apart from the linear response at the forcing frequency, several higher-order harmonics are seen. The inner wall-normal locations ($z^+ \approx 15$ and 60) contain more higher-order harmonics when compared to the outer wall-normal region ($z^+ \approx 60$) at $x/b = 50$ (Fig. 12). With increasing downstream distance the nonlinear, higher-order harmonic response dies out at all wall-normal locations though it prevails to greater downstream locations in the wall region ($z^+ \approx 15$ and 60) than in the outer region ($z \approx 0.6\delta^0$). In the outer region ($z \approx 0.6\delta^0$) the higher

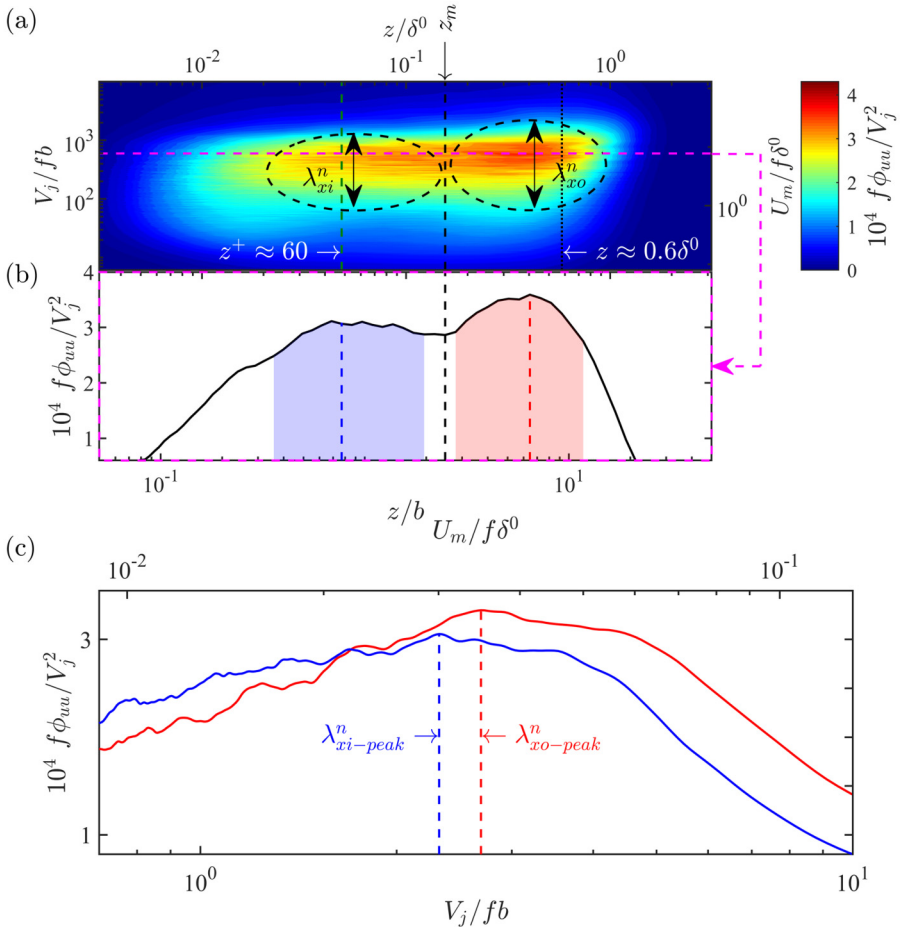

FIG. 13. (a) Spectrogram of the unforced flow at $x/b = 137$. The circled regions indicate wavelength extents of the naturally energetic large-scale structures in the inner (λ^n_{xi}) and the outer (λ^n_{xo}) regions, respectively. The vertical lines show the wall-normal locations $z^+ \approx 60$ (- - - - -), $z \approx z_m$ (- - - - -), and $z \approx 0.6\delta^0$ (.....), respectively. (b) Premultiplied energy spectrum for the wavelength $V_j/fb \approx 600$ (- - - - -) highlighted in figure (a). The shaded regions illustrate the nominal wall-normal extents of λ^n_{xi} (blue) and λ^n_{xo} (red), respectively. The vertical lines show the wall-normal locations of the corresponding inner (- - - - -) and outer (- - - - -) peak energy values, respectively. The vertical line at $z \approx z_m$ (- - - - -) nominally differentiates the wall region from the outer region. (c) Comparison of the energy peaks in the wall region at $z^+ \approx 60$ (blue) and the outer region at $z \approx 0.6\delta^0$ (red). The vertical lines indicate the peak values for inner $\lambda^n_{xi-\text{peak}}$ (- - - - -) and outer $\lambda^n_{xo-\text{peak}}$ (- - - - -), respectively.

harmonics have no energy at $x/b \geqslant 75$, though at $z^+ \approx 15$ and 60 the first harmonic has significant energy at upstream locations and this energy dies out at $x/b = 110$. Also seen is that the linear response at the fundamental forcing frequency f_f persists in the wall layer up to $x/b = 162$ while in the outer region there is very little energy at f_f at streamwise distances $x/b \geqslant 110$.

As the PWJ spreads in extent in the downstream direction the naturally occurring energetic large scales in the both the inner region λ^n_{xi} and the outer region λ^n_{xo} are moving to larger and larger scales. However, the forcing and its energetic linear response are at a single fixed wavelength λ^f_x. Hence, at the most upstream locations ($x/b \leqslant 75$), λ^f_x is larger than the peak in the naturally occurring large scales in both the inner and outer regions ($\lambda^n_{xi-\text{peak}}$ and $\lambda^n_{xo-\text{peak}}$, respectively). As the PWJ develops

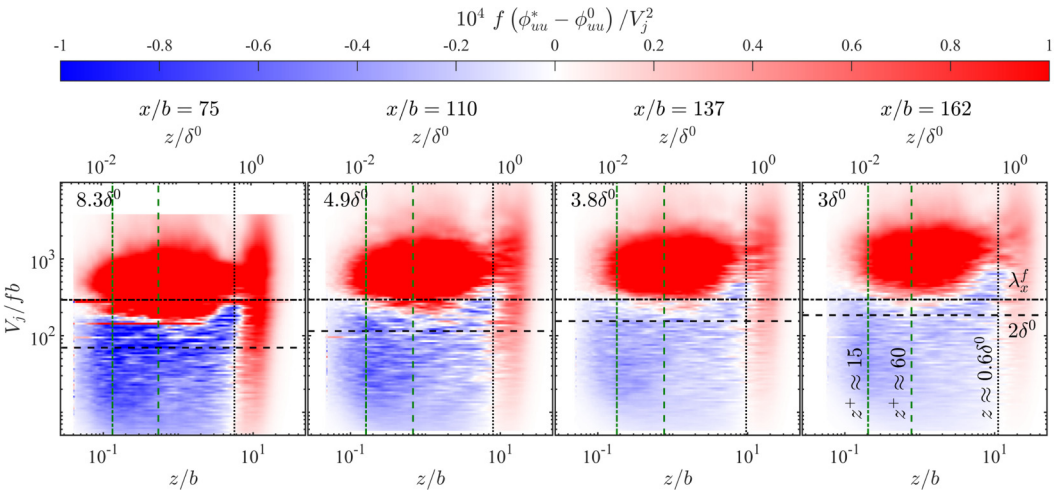

FIG. 14. Downstream development of the difference in the energy spectra between the forced and unforced flow $[f(\phi^*_{uu}-\phi^0_{uu})/V_j^2]$. The vertical lines show wall-normal locations $z^+ \approx 15$ (–·–·–·–) and 60 (– – – –) and $z \approx 0.6\delta^0$ (·····), respectively. The horizontal lines show the cutoff wavelength $\lambda_x = 2\delta^0$ (– – – –) and the forcing wavelength $V_j/f_f b$ (–·–·–·–), respectively. The numbers on the top left corner of each figure show the forcing wavelength nondimensionalized with respect to the outer variables at the respective streamwise location.

further downstream the fixed forcing wavelength λ_x^f (and its linear response at this fixed wavelength) becomes equal to and then eventually smaller than the peak in the naturally occurring large scales of both the inner ($\lambda^n_{xi-\text{peak}}$) and outer ($\lambda^n_{xo-\text{peak}}$) regions. This transition occurs earlier in the outer region when compared to the inner region because, as noted previously, $\lambda^n_{xo-\text{peak}} > \lambda^n_{xi-\text{peak}}$.

This arrangement of the naturally occurring large scales relative to the forcing scale allows for an interesting energy-transfer mechanism in the forced PWJ. Two difference plots are used to aid in this discussion. Figure 14 shows the difference between the spectrograms of the forced and unforced flow as a function of downstream distance. Figure 15 shows the difference between the spectrograms at a given streamwise location and the immediate upstream location. The line plots of the premultiplied energy spectra at $z^+ \approx 15$ and 60 and $z \approx 0.6\delta^0$, as shown in Fig. 12, also allow for a visual comparison of the relative scale sizes of the forced and unforced flow at a given streamwise location.

The difference between the forced and unforced flow at a fixed streamwise location is first considered. It is observed that energy at the forcing wavelength λ_x^f is primarily transferred to the large scales of the flow ($\lambda_x > 2\delta^0$) that reside at a specific wall-normal region. It is seen that these recipient scales reside primarily in the logarithmic region of the PWJ. This reinforces the observations of the turbulence intensity plot of Fig. 6 where the dominant increase in energy is seen in the large scales that lie below z_m. The recipient wavelengths, referred to as λ_x^r for the rest of this discussion, move to larger and larger wavelengths with increasing downstream location. Here again, it is noted that λ_x^r refers to a range of wavelengths.

Restricting for the moment the discussion to the wall region, at the most upstream locations $x/b \leqslant 110$, $\lambda_x^f > \lambda^n_{xi-\text{peak}}$. In this case the energy from λ_x^f and its harmonics are transferred to λ_x^r with λ_x^r spanning wavelengths greater than and less than λ_x^f. Hence the energy at λ_x^f is being depleted to scales larger than itself in the manner of an inverse cascade as well as to scales smaller than itself through a forward cascade. In the case of the higher harmonics of λ_x^f, the energy transfer is in the direction of an inverse cascade as the higher harmonics of λ_x^f are smaller than λ_x^r. At further

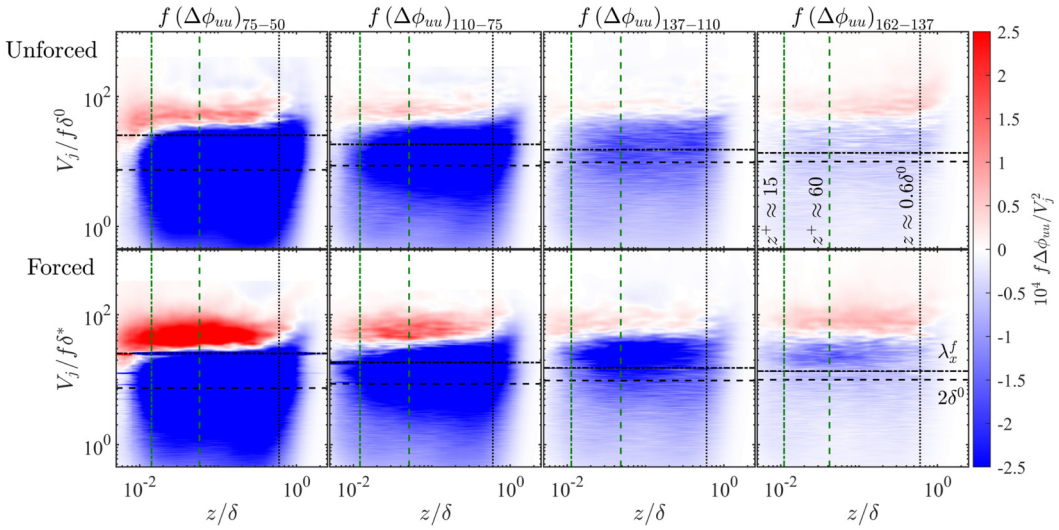

FIG. 15. Difference of premultiplied energy spectra between a streamwise location and the immediately preceding downstream location corresponding to both the unforced (top) and forced (bottom) flow. The vertical lines show the wall-normal locations $z^+ \approx 15$ (-·-·-·-) and 60 (- - - - -) and $z \approx 0.6\delta^0$ (·····), respectively, at the upstream location. The horizontal lines show the forcing wavelength $V_j/f_f b$ (-·-·-·-) and the cutoff frequency $\lambda_x = 2\delta^0$ (- - - - -). Here, the axes are nondimensionalized by the respective local shear-layer thickness δ.

downstream locations $x/b \geqslant 137$, the energy transfer is almost exclusively to scales larger than λ_x^f indicative of an inverse cascade. In the outer region there is no increase in the large-scale energy up to $x/b = 75$ (except at λ_x^f and its harmonics). When $x/b \geqslant 110$ there is a small increase in the energy of scales larger than λ_x^f again indicative of an inverse cascade.

Considering the small-scale energy $\lambda_x < 2\delta^0$, at all streamwise distances there is a decrease in small-scale energy in the forced flow with respect to the unforced flow at wall-normal locations $z \lessapprox 0.6\delta^0$, whereas at higher wall-normal locations there is an increase in small-scale energy (see Fig. 14). Particularly in the near-wall region $z^+ \approx 15$ (see line plots of Fig. 12) the reduction in energy of the small scales is consistent and more significant.

The difference in energy between streamwise distances (Fig. 15) for the forced and unforced flow is now considered. A line plot of this difference at the three reference wall-normal locations is also shown in Fig. 16. In the case of the unforced flow, the energies in the large scales are increasing concomitant with an increase in downstream direction as the larger scales are getting larger. Comparing the unforced and forced flows it is clear that the regions of increased energy and depleted energy are nearly identical (except at the forcing wavelength λ_x^f). This is highlighted in the line plot of Fig. 16. It is seen that the regions of increased and decreased energy as the flow develops downstream are identical in the forced and unforced flow, with the forced flow exhibiting a larger magnitude of changes attributed to the available excess energy due to forcing. This suggests that the energy transfer due to forcing follows the natural energy-transfer mechanism within the PWJ. In other words, the forcing isolates the energy-transfer mechanism within the PWJ due to a single wavelength, i.e., the forcing wavelength λ_x^f. The forcing and its linear response provide excess energy at this wavelength; this excess energy then follows the naturally occurring energy-transfer pathway within the flow. This strengthens the argument that the forcing linear response mimics naturally occurring scales of the flow at the forcing frequency.

Turning the attention once again to the energy spectra line plots of Fig. 12, a final observation is made. At plots corresponding to the wall-normal locations $z^+ \approx 15$ and 60, along with the profiles

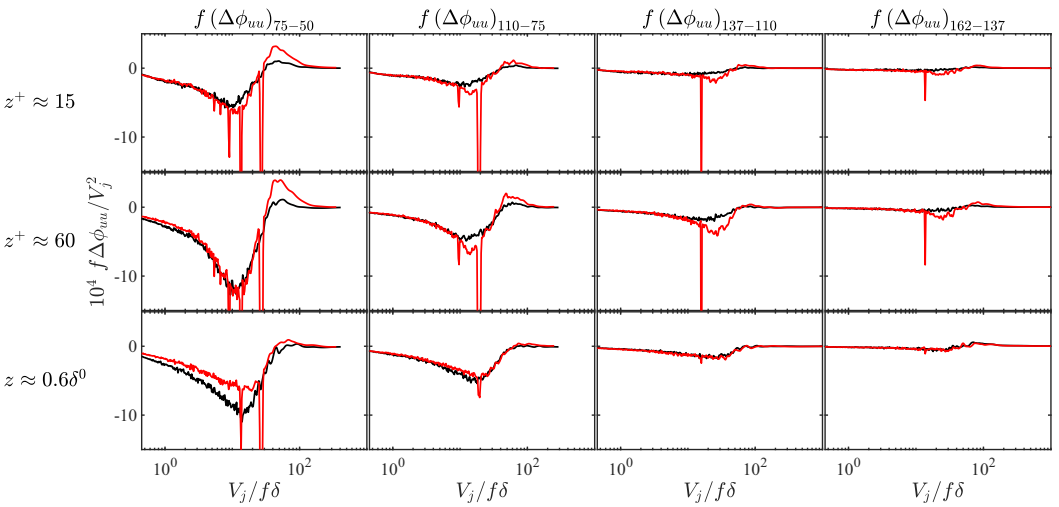

FIG. 16. Line plots of the energy difference shown in Fig. 15 at three wall-normal locations $z^+ \approx 15,\ 60,$ and $0.6\delta^0$. Black lines (———) are used to represent the unforced flow, whereas the red lines (———) represent the forced flow. Here, the axes are nondimensionalized by the respective to the local shear-layer thickness δ.

of the premultiplied energy spectra $f\phi_{uu}$ of both the forced and unforced flow at $z^+ \approx 15$ and 60, the unforced spectrum at $z \approx 0.6\delta^0$ is also shown. It is observed that the recipient scale λ_x^r while residing primarily in the wall region has a peak that corresponds to the peak of the naturally occurring outer scales, i.e., $\lambda^r_{x-\text{peak}} \approx \lambda^n_{xo-\text{peak}}$. In other words the excess energy upon forcing is being transferred to the scales of the size of the naturally occurring outer scales λ^n_{xo}, though these recipient scales primarily reside in the wall region. In the outer regions of the flow ($z \approx 0.6\delta^0$) the line plots of Fig. 12 show that the effect of forcing at streamwise locations $x/b \geqslant 110$ is to slightly increase the overall energy in the large scales while in this case the recipient scales are marginally larger than $\lambda^n_{xo-\text{peak}}$.

G. Scale interactions

In canonical boundary layers the outer larger scales have been observed to interact with the finer scales through a process of amplitude and frequency modulation [29]. This amplitude modulation effect is quantified using the amplitude modulation coefficient R_{AM} as given by Mathis *et al.* [30]:

$$R_{\text{AM}} = \frac{\overline{U_L E_L(U_s)}}{\sqrt{\overline{U_L^2}}\sqrt{\overline{E_L(U_s)^2}}}. \tag{3}$$

Here, U_L and U_s are the large-scale and small-scale components of the streamwise velocity, respectively, while E_L is the large-scale component of the envelope of U_s calculated using the Hilbert transform. The cutoff wavelength to separate the large scales from the small scales is $\lambda_x = 2\delta^0$. Figure 17 shows the profiles of the amplitude modulation coefficient R_{AM} as a function of streamwise locations for the unforced and the forced flows. In the case of the unforced flow the large scales are seen to amplitude modulate the finer scales across the entire layer at all streamwise locations. In the near-wall region, as the flow develops downstream, this modulation increases. At $x/b = 50$, when $z^+ \approx 15$, $R_{\text{AM}} \approx 0.34$ in the case of the unforced flow. This increases to $R_{\text{AM}} \approx 0.41$ at $x/b = 162$, indicating a naturally increasing modulation effect in the near-wall region as the flow develops downstream.

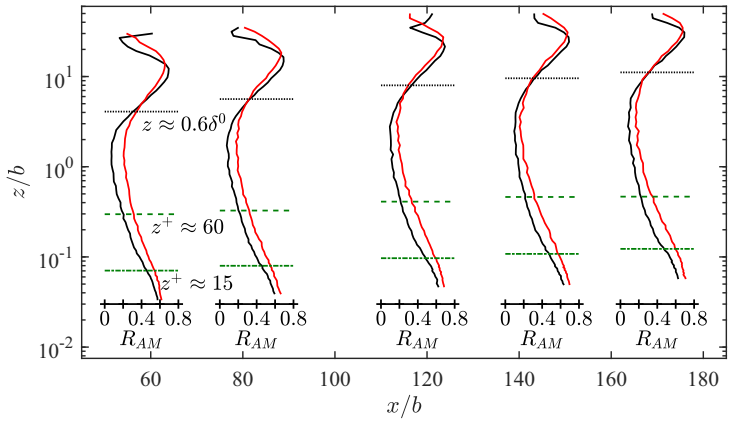

FIG. 17. Variation of the amplitude modulation coefficient R_{AM} (———) as the flow develops downstream. The black color represents the unforced flow and the red color represents the forced flow. The horizontal lines highlight the wall-normal locations $z^+ \approx 15$ (–·–·–·–) and 60 (- - - -) and $z \approx 0.6\delta^0$ (·····), respectively.

The modulation increases upon forcing in the region $z \lessapprox 0.6\delta^0$ at all streamwise locations considered. However, it remains relatively unaffected in the outer region ($z \gtrsim 0.6\delta^0$), with only a shift due to the increased spreading of the PWJ. At each streamwise location, at $z^+ \approx 15$, the R_{AM} approximately increases by ≈46% upon forcing. This increase is attributed to the more energetic large scales in the forced flow. The increased large-scale energy at the forcing frequency (the linear response) and the resulting cascade of the excess energy both cause the increased modulation. This is highlighted in Fig. 18 where only the modulation effect at the forcing frequency f_f is shown for both the forced and the unforced flow at $x/b = 137$. It is noted that this figure is exemplary of other streamwise locations as well. A narrow spectral, cutoff bandpass filter ($f_f \pm 0.01$ Hz) was first used

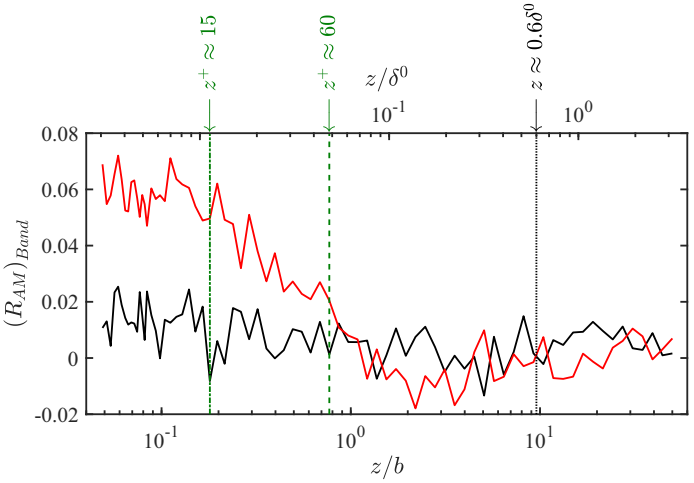

FIG. 18. The profiles of the amplitude modulation coefficient $(R_{\mathrm{AM}})_{\mathrm{Band}}$ at $x/b = 137$ showing only the contribution at the forcing frequency f_f. The black color represents the unforced flow and the red color represents the forced flow. The vertical lines show the wall-normal locations $z^+ \approx 15$ (–·–·–·–) and 60 (- - - -) and $z \approx 0.6\delta^0$ (·····), respectively.

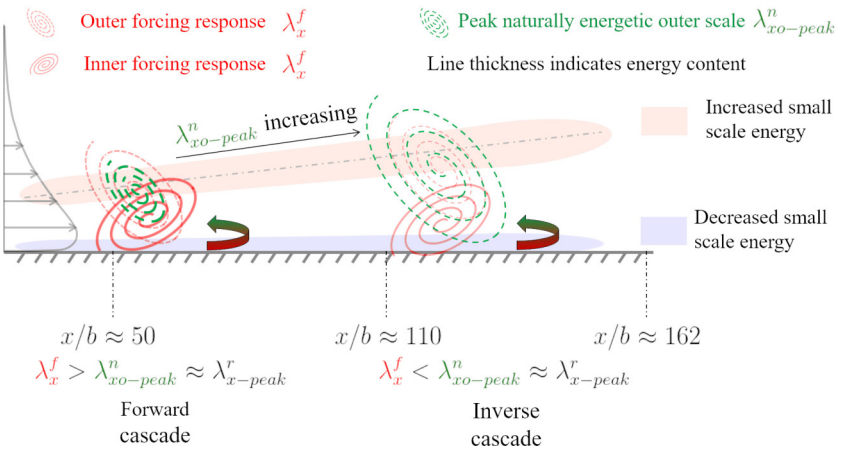

FIG. 19. A schematic highlighting the key mechanisms in the forced plane wall jet. Shown are the linear response, the direction of energy transfer, and the recipient scales.

to isolate the large scales at the forcing frequency. The modulation effect due to this large scale was then calculated using Eq. (2) where U_L was now the bandpass filtered velocity. Comparing the forced and unforced flow modulation coefficients, the flow structures at the forcing frequency f_f cause $(R_{\mathrm{AM}})_{\mathrm{Band}}$ to increase from nearly zero to 0.06 in the near-wall region. We interpret this as the linear response having a modulating effect on the smaller scales. Chung and McKeon [31] highlight that the modulation coefficient R_{AM} is also the phase difference between the envelope of the large scales and the finer scales. In other words R_{AM} is reflective of the relative scale organization within a flow. Therefore, a positive R_{AM} would indicate that the large scales are in phase with finer scales and vice versa. Hence, another interpretation of the increase in $(R_{\mathrm{AM}})_{\mathrm{Band}}$ is that the flow scale associated with the linear response organizes the base flow about itself, particularly in the near-wall region, leading to an increase in $(R_{\mathrm{AM}})_{\mathrm{Band}}$.

IV. DISCUSSION

First, the key observations of the presented works are summarized. An interpretation explaining these observations is then offered followed by a discussion of the implications. To assist in this process a schematic highlighting the key mechanisms is shown in Fig. 19. Large-scale, large-amplitude perturbations were used to force a PWJ. The linear response of the PWJ to the forcing resulted in flow features with strong similarities to the naturally occurring flow structures in the PWJ (red structures in Fig. 19). The inner response flow features were forward leaning, showing similarities to boundary-layer-like structures seen in the wall region of the unforced PWJ. On the other hand the outer flow features of the linear response were backward leaning like those of the free-shear layer structures in the outer regions of the unforced PWJ. The energies in the wall linear response flow features were larger than those of the outer ones at all streamwise locations considered. It is also noted here that the scale interactions within the forced flow indicated that the flow structures associated with the linear response had a modulating or organizing effect on the near-wall flow. The linear response of the flow to the forcing resulted in excess energy, at the forcing frequency, at a given streamwise location. This excess energy then gets transferred to the other scales of the flow at further downstream locations. It was observed that depending on the streamwise location the direction of energy transfer varied, i.e., the excess energy was transferred to scales larger than the forcing scale (at downstream locations) or vice versa (at upstream locations). This transfer direction is also highlighted in the schematic of Fig. 19. Despite the direction of energy transfer, the recipient scales had a peak in the streamwise wavelength that was identical to those of the outer

shear layer structures (green structures in Fig. 19). From comparing the spectra of the forced and unforced flow it was observed that, as the flow develops downstream, the scales of increasing and decreasing energy remain unchanged from the forced and unforced flow. The wall-normal regions on increasing and decreasing energy also remained unchanged. Only the energy magnitude was increased in the case of the forced flow, which was expected as the forced flow has more energy.

Based on these observations, the following interpretations or inferences are offered. The excess energy of forcing resided primarily in the forward leaning wall linear-response flow features. This excess energy was transferred to the flow scales the streamwise wavelengths of which match those of the outer free-shear layer structures, which suggests that the energies from the wall response flow features were transferred to the naturally occurring outer free-shear layer structures. However, the spectra comparing the forced and unforced flow showed that the wall-normal regions and scales of increasing and decreasing energy were identical with only the relative energy magnitudes being different. This then suggests that whatever natural processes or forcing occurred within the forced plane wall jet also existed in the unforced one. Together these interpretations are combined and it is argued that the flow features associated with the linear response of the flow mimic the naturally occurring structures at the forcing wavelength. This in turn leads to the interpretation that the near-wall structures in a PWJ are naturally transferring energy from the near-wall structures to the outer free-shear layer structures. Hence, the imposed large-scale, large-amplitude forcing isolates a naturally occurring energy-transfer pathway within the flow where the excess energy is supplied at the forcing frequency.

The preceding observations reinforce the view that the PWJ is a complex, wall-bounded flow characterized by significant turbulent transport and scale interactions. The transfer of energy from the linear-response structures in the wall-normal to the outer scales indicates that the natural mechanism within the PWJ is to transfer energy from the near-wall coherent structures to the free-shear layer coherent structures. This energy transfer between the coherent structures is primarily in the manner of an inverse cascade as the two-point correlations of the unforced PWJ [1] show that the free-shear layer structures are larger than the wall-layer structures. However, this transfer between scales occurs in the wall region, suggesting that the outer free-shear layer structures intrude well into the wall region.

Several past works have studied the linear dynamics of the Navier-Stokes equation, linearized about the turbulent mean velocity profile (see the recent review by McKeon [27]). Using the resolvent framework [32,33], based on the input-output analysis of laminar flows [34], predictions of the large-scale structures within canonical turbulent boundary layers were made. These resolvent modes capture well the structural features of the actual flow [33]. In the resolvent framework these large-scale modes are determined by subjecting the linear portion of the Navier-Stokes equation to forcing by the flow nonlinearities, the underlying argument being that the linear portion of the Navier-Stokes equation, constrained by the turbulent mean velocity profile, acts as a highly selective dynamical system. In a related work, Madhusudanan *et al.* [35] used the linearized Navier-Stokes equation, where an eddy viscosity is used in conjunction with the kinematic viscosity, to predict the large-scale features of a channel flow. Here, following the resolvent framework, stochastic white-in-time forcing is used to force the linearized Navier-Stokes equation. This approach captured well the large-scale coherence spectrum when compared with that derived from a DNS.

Following this linear systems based perspective, the linear response of any large-amplitude forcing of an experimental flow would result in flow eddies that mimic the naturally present ones in the unforced flow, at the forcing frequency. The present results are thus consistent with this framework. It is also noted that the mean velocity profile of the PWJ is unaltered by the large-scale forcing; i.e., it is still self-similar. Hence, as the linear response results in large-scale features that are similar to the naturally occurring flow features, this supports the view that the shape of the mean velocity profile is the primary factor that determines the shape of the resulting flow features. In other words, an unchanged mean velocity profile limits the resulting possible flow structures, or put yet another way the forcing produces flow features that mimic the existing flow features at the forcing wavelength.

In the case of the resolvent approach the nonlinearities in the flow only act to redistribute the energy between flow scales. This occurs in a triadically consistent manner, as dictated by the quadratic nature of the Navier-Stokes equation. Particularly, the present paper highlights all energy-transfer mechanisms within a naturally interacting flow field in which the forcing wave number always forms one leg of the triad. The present paper then suggests that this redistribution is expectedly nontrivial and in need of "rules," which includes the direction of the energy transfer. The use of an eddy viscosity provides one such set of rules, however this implicitly assumes a forward energy cascade. This approach would also perform poorly in flows such as the PWJ where there are regions of low production and energy is transported from one spatial location to another [15]. This is consistent with past work on the PWJ where turbulence models have performed poorly in modeling the PWJ [15]. Dejoan *et al.* [15] use a nonlinear eddy viscosity to model the PWJ which compares well with budgets derived from an LES approach, and perhaps provides a way forward for modeling flows with internal interactions and transport such as the PWJ.

To summarize, the current paper presents evidence to support the viewpoint that large-scale features of turbulent flows are described well by the dynamics of the linear portion of the Navier-Stokes equation. However, the scale interaction dictated by the nonlinearities of the flow is complex and requires careful treatment, which is the subject of ongoing research. From a flow physics standpoint, the PWJ is a complex flow field which has at least two types of interacting flow features which are boundary-layer-like and jetlike. The PWJ naturally supports an interaction between these two structures. While the wall layer forms stronger structures, as part of the linear response, the outer shear layer structures then receive this excess energy, supported by the naturally occurring turbulent transport within the flow. Hence, there is a natural transfer of energy between two types of coherent structures which has been isolated and highlighted by the forcing. There is yet another factor that has not been considered, which is the spanwise energy transfer. This transfer is not insignificant as highlighted by the DNS study of a PWJ [14]. Current work is focused on a particle image velocimetry based study to characterize this transfer.

V. CONCLUSIONS

A PWJ was subject to large-amplitude forcing at a $\mathrm{St} = 3.4\times10^{-3}$ at a nominal Reynolds number $\mathrm{Re}_j = 5965$. The forcing considered was a large-scale input to the flow such that the response produced was both linear and nonlinear. The following observations and conclusions were made. The forced PWJ retained a self-similar streamwise mean velocity profile. However, the forced flow showed an increase in the outer length scale δ and a decrease in the outer velocity scale U_m at all streamwise locations considered. Together these changes result in an increased local Reynolds number. The streamwise turbulence intensity profile showed a large increase, predominantly in the wall layer of the flow. These recipient scales in the wall layer were primarily the large scales. The forcing resulted in a reduction in the friction velocity at all streamwise locations considered. The wall layer of the forced PWJ showed a reduction in momentum while the overall momentum of the PWJ increased.

The linear response of the PWJ to the forcing resulted in flow structures that bore strong similarities to the naturally occurring large-scale features in the unforced flow. These include boundary-layer-like flow features in the inner wall layer and free-shear-layer-like flow features in the outer region. This excess energy in the linear response gets transferred to other flow scales driven by the flow nonlinearities as the flow develops downstream. These recipient scales are primarily the large scales of the flow which reside in the wall layer. However, the sizes of these scales were those of the outer free-shear layer. Furthermore, this transfer of energy was either in the manner of a forward cascade or inverse cascade. This direction of transfer was dependent on the streamwise location with the forward energy transfer occurring at upstream locations. The spectra showed that these energy-transfer mechanisms mimic the naturally occurring energy-transfer mechanisms within the unforced flow. Hence, it is concluded that the forcing isolates an energy-transfer pathway within the PWJ, where the input energy is at the forcing frequency.

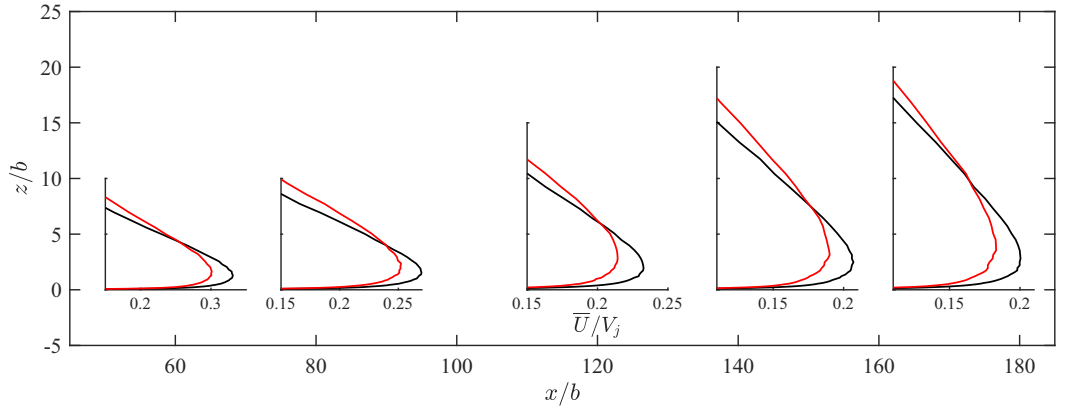

FIG. 20. Zoomed-in mean streamwise velocity profiles of the unforced (——) and forced (——) flow shown in Fig. 5.

ACKNOWLEDGMENT

The authors would like to thank the US Air Force Office of Scientific Research (Grant No. FA9550-16-1-0194) for their financial support for this project.

APPENDIX A: ZOOMED-IN STATISTICS

Figures 20 and 21 show zoomed-in profiles of the mean streamwise velocity and turbulence intensity, respectively.

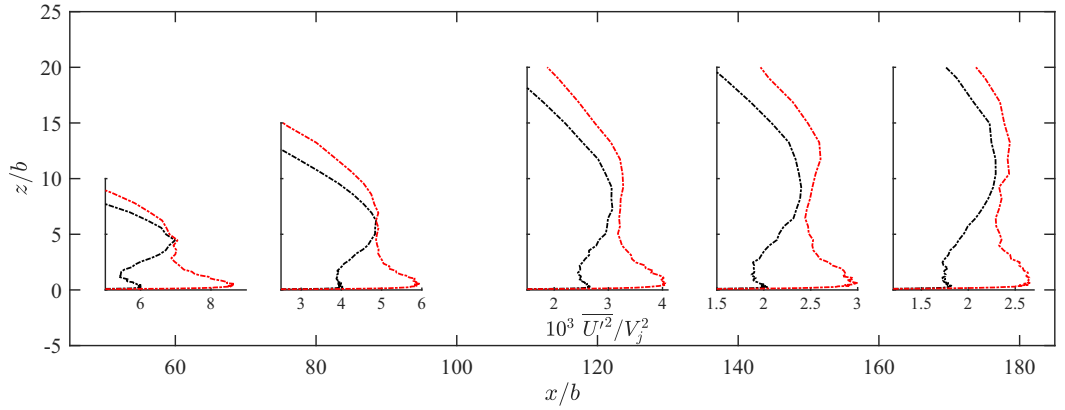

FIG. 21. Zoomed-in streamwise turbulence intensity profiles of the unforced (–·–·–) and forced (–·–·–) flow shown in Fig. 5.

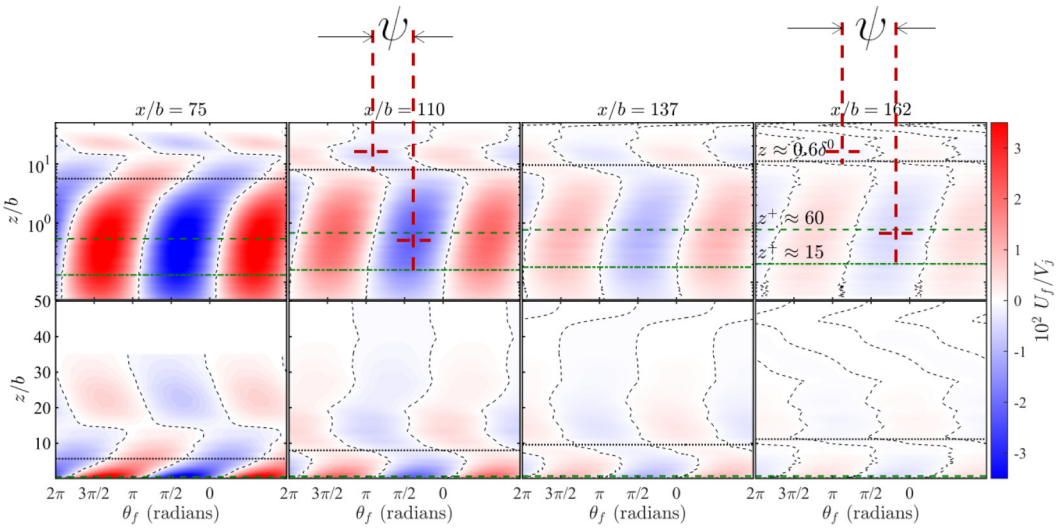

FIG. 22. Variation of the phase-locked velocity U_f [see Eq. (2)] over two forcing cycles shown in logarithmic (top) and linear (bottom) wall-normal coordinates. The streamwise distance increases going from left to right. The color contours are the magnitude of U_f as indicated by the color bar. The contour level corresponding to $U_f = 0$ is also shown. The horizontal lines show wall-normal locations $z^+ \approx 15$ (-·-·-·-) and 60 (- - - - -) and $z = 0.6\delta^0$ (·····), respectively. This figure is identical to Fig. 9, except that the velocity field was filtered to isolate the response associated with the fundamental forcing frequency, filtering out the higher harmonics. Ψ shows the relative phase between the near-wall response feature and the middle response feature.

APPENDIX B: FILTERED U_f

A filtered version of Fig. 9 is shown in Fig. 22, where only the linear-response portion of U_f was isolated.

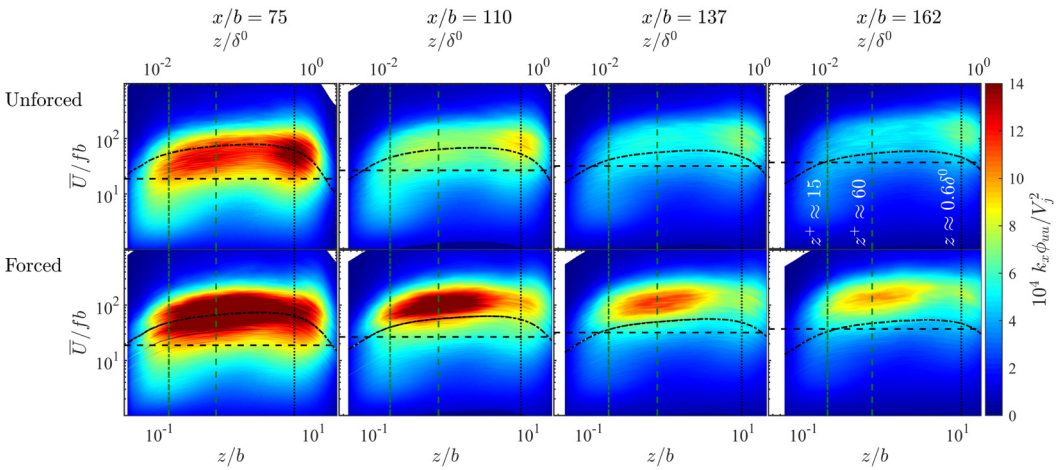

FIG. 23. Contour maps of the streamwise, one-dimensional, premultiplied energy spectra $k_x\phi_{uu}/V_j^2$ for the unforced (top) and the forced (bottom) flow conditions. Here, the local mean streamwise velocity is used as the convective velocity in Taylor's hypothesis to convert a flow frequency into a wavelength. The streamwise development is shown from left to right. The vertical lines show the wall-normal locations $z^+ \approx 15$ (-·-·-·-) and 60 (- - - - -) and $z \approx 0.6\delta^0$ (·····), respectively. The forcing wavelength $\overline{U}/f_f b$ (-·-·-·-) is highlighted for reference.

APPENDIX C: ENERGY SPECTRA

For reference, the spectra corresponding to Fig. 11 using Taylor's hypothesis and the local mean velocity as the convection velocity are shown in Fig. 23.

[1] E. P. Gnanamanickam, S. Bhatt, S. Artham, and Z. Zhang, Large-scale motions in a plane wall jet, J. Fluid Mech. **877**, 239 (2019).

[2] A. Dejoan and M. A. Leschziner, Large eddy simulation of a plane turbulent wall jet, Phys. Fluids **17**, 1 (2005).

[3] I. Wygnanski, Y. Katz, and E. Horev, On the applicability of various scaling laws to the turbulent wall jet, J. Fluid Mech. **234**, 669 (1992).

[4] B. E. Launder and W. Rodi, The turbulent wall jet measurements and modeling, Annu. Rev. Fluid Mech. **15**, 429 (1983).

[5] A. Dejoan and M. A. Leschziner, On the near-wall structure in reverse-flow and post-reattachment recovery regions of separated flow and its equivalence to the structure in wall and free-surface jets, J. Turbul. **8**, N14 (2007).

[6] B. E. Launder and W. Rodi, The turbulent wall jet, Prog. Aerosp. Sci. **19**, 81 (1981).

[7] M. E. Schneider and R. J. Goldstein, Laser Doppler measurement of turbulence parameters in a two-dimensional plane wall jet, Phys. Fluids **6**, 3116 (1994).

[8] H. Abrahamsson, B. Johansson, and L. Löfdahl, A turbulent plane two-dimensional wall-jet in a quiescent surrounding, Eur. J. Mech. B: Fluids **13**, 533 (1994).

[9] J. G. Eriksson, R. I. Karlsson, and J. Persson, An experimental study of a two-dimensional plane turbulent wall jet, Exp. Fluids **25**, 50 (1998).

[10] N. Rostamy, D. J. Bergstrom, D. Sumner, and J. D. Bugg, The effect of surface roughness on the turbulence structure of a plane wall jet, Phys. Fluids **23**, 085103 (2011).

[11] Y. Katz, E. Horev, and I. Wygnanski, The forced turbulent wall jet, J. Fluid Mech. **242**, 577 (1992).

[12] M. D. Zhou, C. Heine, and I. Wygnanski, The effects of excitation on the coherent and random motion in a plane wall jet, J. Fluid Mech. **310**, 1 (1996).

[13] R. Banyassady and U. Piomelli, Interaction of inner and outer layers in plane and radial wall jets, J. Turb. **16**, 460 (2015).

[14] I. Z. Naqavi, J. C. Tyacke, and P. G. Tucker, Direct numerical simulation of a wall jet: Flow physics, J. Fluid Mech. **852**, 507 (2018).

[15] A. Dejoan, C. Wang, and M. A. Leschziner, Assessment of turbulence models for predicting the interaction region in a wall jet by reference to LES solution and budgets, Flow Turbul. Combust. **77**, 229 (2006).

[16] W. K. George, H. Abrahamsson, J. Eriksson, R. I. Karlsson, L. Löfdahl, and M. Wosnik, A similarity theory for the turbulent plane wall jet without external stream, J. Fluid Mech. **425**, 367 (2000).

[17] A. Dejoan and M. A. Leschziner, Separating the effects of wall blocking and near-wall shear in the interaction between the wall and the free shear layer in a wall jet, Phys. Fluids **18**, 065110 (2006).

[18] I. Jacobi and B. McKeon, Dynamic roughness perturbation of a turbulent boundary layer, J. Fluid Mech. **688**, 258 (2011).

[19] I. Jacobi and B. J. McKeon, New perspectives on the impulsive roughness-perturbation of a turbulent boundary layer, J. Fluid Mech. **677**, 179 (2011).

[20] I. Jacobi and B. J. McKeon, Phase relationships between large and small scales in the turbulent boundary layer, Exp. Fluids **54**, 1481 (2013).

[21] S. Duvvuri and B. J. McKeon, Triadic scale interactions in a turbulent boundary layer, J. Fluid Mech. **767**, R4 (2015).

[22] S. Duvvuri and B. McKeon, Nonlinear interactions isolated through scale synthesis in experimental wall turbulence, Phys. Rev. Fluids **1**, 032401 (2016).

[23] B. J. McKeon, I. Jacobi, and S. Duvvuri, Dynamic roughness for manipulation and control of turbulent boundary layers: An overview, AIAA J. **56**, 2178 (2018).
[24] M. Schober and H.-H. Femholz, Turbulence control in wall jets, Eur. J. Mech. B: Fluids **19**, 503 (2000).
[25] N. Hutchins, T. B. Nickels, I. Marusic, and M. S. Chong, Hot-wire spatial resolution issues in wall-bounded turbulence, J. Fluid Mech. **635**, 103 (2009).
[26] A. M. F. K. Hussain and C. Reynolds, The mechanics of an organized wave in turbulent shear flow, J. Fluid Mech. **41**, 241 (1970).
[27] B. J. McKeon, The engine behind (wall) turbulence: Perspectives on scale interactions, J. Fluid Mech. **817**, P1 (2017).
[28] S. J. Illingworth, J. P. Monty, and I. Marusic, Estimating large-scale structures in wall turbulence using linear models, J. Fluid Mech. **842**, 146 (2018).
[29] R. Mathis, J. P. Monty, N. Hutchins, and I. Marusic, Comparison of large-scale amplitude modulation in turbulent boundary layers, pipes, and channel flows, Phys. Fluids **21**, 1 (2009).
[30] R. Mathis, N. Hutchins, and I. Marusic, Large-scale amplitude modulation of the small-scale structures in turbulent boundary layers, J. Fluid Mech. **628**, 311 (2009).
[31] D. Chung and B. J. McKeon, Large-eddy simulation of large-scale structures in long channel flow, J. Fluid Mech. **661**, 341 (2010).
[32] B. McKeon and A. Sharma, A critical-layer framework for turbulent pipe flow, J. Fluid Mech. **658**, 336 (2010).
[33] B. J. McKeon, A. S. Sharma, and I. Jacobi, Experimental manipulation of wall turbulence: A systems approach, Phys. Fluids **25**, 031301 (2013).
[34] M. R. Jovanović and B. Bamieh, Componentwise energy amplification in channel flows, J. Fluid Mech. **534**, 145 (2005).
[35] A. Madhusudanan, S. J. Illingworth, and I. Marusic, Coherent large-scale structures from the linearized Navier-Stokes equations, J. Fluid Mech. **873**, 89 (2019).